

TILTING OF A DISK OF GRAVITATING RINGS

R.V.E. Lovelace

Department of Astronomy, Cornell University, Ithaca, NY 14853-6801; rvl1@cornell.edu

ABSTRACT

The present work represents an attempt to understand the ‘rules of behavior’ of observed warps in the HI disks of spiral galaxies found by Briggs (1990). In contrast with most earlier theoretical work, the present study investigates different initial value problems of a warped disk in an oblate (or prolate) halo potential, and it represents the disk warp in terms of N independently tilted, self-gravitating, concentric rings. This representation gives new insight into the disk warping. A new constant of the motion of N tilted rings is identified (in addition to the energy). The phenomenon of phase-locking of the lines-of-nodes of nearby rings due to self-gravity is demonstrated. We consider the influence of dynamical friction due to ring motion through the halo matter as well as friction between gaseous rings with different vertical motions due to turbulent viscosity. We first consider the dynamics of one, two, and three tilted rings of different radii in a halo potential. We go on to develop dynamical equations for N -rings which are most simply expressed in terms of the complex tilt angles $\Theta_j = \theta_j \exp(-i\varphi_j)$, where θ_j is the actual tilt angle and φ_j the line-of-nodes angle for the j^{th} ring ($j = 1..N$). We numerically solve the equations for Θ_j for four different types of initial conditions: (1) warp excitation by a passing satellite, (2) excitation by a sinking compact minor satellite, (3) warp evolution due to a tilted halo potential, and (4) warp evolution resulting from an initially tilted disk plane.

Subject headings: accretion, accretion disks—instabilities— galaxies: kinematics and dynamics

1. Introduction

The large-scale integral-sign warps of the outer regions of spiral galaxies has been a long-standing theoretical puzzle. The strongest warps are observed in the HI disks when these extend well beyond the optical disks (Briggs 1990). The warps are antisymmetric and consequently can be well-fitted by the kinematic tilted-ring model of Rogstad, Lockhart, and Wright (1974). For a set of 12 galaxies with high-quality data on the extended HI disks, Briggs (1990) found empirically a set of ‘rules of behavior’ of warps: 1. The warps develop with increasing radius r for r between R_{25} and R_{Hol} (the Holmberg radius, $= R_{26.5}$), where the subscript denotes the surface brightness in B in mag/arcsec²; 2. The line-of-nodes of the warp is straight for $r < R_{Hol}$; and 3. For $r > R_{Hol}$, the line-of-nodes forms an open leading spiral. An illustrative case is shown in Figure 1 which gives a surface plot of the warp of the disk of the spiral galaxy M 83 obtained from the data of Briggs (1990). The rotation of M 83 is clockwise so that the warp is a *leading* spiral wave. Figure 2 also shows the data of Briggs (1990) for M 83, in panel (a) the radial (r) dependence of the tilt angle θ , in (b) the r -dependence of the angle of the line-of-nodes φ , and in (c) the dependence of θ on φ , which we refer to as a Briggs plot. A different behavior is observed for the galaxy NGC 3718 which shows an approximately straight line-of-nodes out to $r \approx 1.75R_{Hol}$ and a large tilt angle ($\sim 90^\circ$) at this radius (Briggs 1990).

A partial listing of the theoretical works on warps of disk galaxies include Kahn and Woltjer (1959), Hunter and Toomre (1969; hereafter HT), Toomre (1983), Sparke and Casertano (1988), Binney 1992, Hunter (1994), Merritt and Sellwood (1994), and Nelson and Tremaine (1995). Since the pioneering analysis by Hunter and Toomre (1969) and the earlier related work by Lynden-Bell (1965), the theoretical studies have focused mainly on determining the eigenmodes and eigenfrequencies of warped self-gravitating disks. The studies used the HT dynamical equation for the vertical displacement of the disk surface $h(r, \phi, t)$, where ϕ is the azimuthal angle.

In contrast with these earlier works, the present study investigates different initial value problems of a warped disk in an oblate (or prolate) halo potential, and it develops a different representation for the disk warping. Instead of describing the disk in terms of $h(r, \phi, t)$, we develop a representation in terms of N

independently tilted, self-gravitating, concentric rings which is suggested by the kinematic ring model of Rogstad et al. (1974). May and James (1984) mention a model of this kind, but they give no details. We show that the N -ring representation is equivalent to the HT equation for $h(r, \phi, t)$ for $N \rightarrow \infty$. However, new insight is given by the N -ring model: A new constant of the motion for a warped disk is found. The notion of the phase-locking of the line-of-nodes of nearby rings due to self-gravity is demonstrated. We propose that this explains Briggs’s rule No. 2. Furthermore, treatment of initial value problems for the age of a galaxy can be done with sufficient accuracy with relatively small values of N ($\lesssim 10^2$).

In §2 we first give basic parameters of the disk and the halo. In §2.1 we treat the case of one tilted ring and in §2.2 comment on the interpretation of observations of a ring. Subsection 2.3 considers the case of two tilted rings. Subsection 2.4 treats the case of two tilted, counter-rotating rings. Subsection 2.5 treats the case of three corotating rings. Section 3 treats the general case of N tilted corotating rings. In this Section we consider different possible excitations or origins of warps - that due to a passing satellite (§3.1), a sinking satellite (§3.2), a tilted halo potential (§3.3), and an initially tilted outer disk plane (§3.4). Section 4 discusses the continuum limit where $N \rightarrow \infty$. Section 5 gives conclusions of this work.

2. Tilting of Disk Galaxies

The equilibrium, unwarped galaxy is assumed to be axisymmetric and to consist of a thin disk of stars and gas and a slightly oblate or prolate halo of dark matter. We use an inertial cylindrical (r, ϕ, z) and Cartesian (x, y, z) coordinate systems with the disk and halo equatorial planes in the $z = 0$ plane. The total gravitational potential is written as

$$\Phi(r, z) = \Phi_{id} + \Phi_{od} + \Phi_h, \quad (1)$$

where Φ_{id} is the potential due to the inner part of the disk (as discussed below), Φ_{od} is that for the outer disk, and Φ_h is that for the halo. The particle orbits in the equilibrium disk are approximately circular with angular rotation rate $\Omega(r)$, where

$$\Omega^2(r) = \left. \frac{1}{r} \frac{\partial \Phi}{\partial r} \right|_{z=0} = \Omega_{id}^2 + \Omega_{od}^2 + \Omega_h^2. \quad (2)$$

The vertical epicyclic frequency (squared),

$$\kappa_z^2(r) \equiv \left. \frac{\partial^2 \Phi}{\partial z^2} \right|_{z=0} = \kappa_{idz}^2 + \kappa_{odz}^2 + \kappa_{hz}^2, \quad (3)$$

gives a measure of the restoring force in the z -direction.

The surface mass density of the inner (optical) disk is assumed to be $\Sigma = \Sigma_0 \exp(-r/r_d)$ with Σ_0 and r_d constants and $M_d = 2\pi r_d^2 \Sigma_0$ the total disk mass. For $r^2 \gg r_d^2$,

$$\begin{aligned} \Omega_{id}^2 &= \frac{GM_d}{r^3} \left(1 + \frac{9}{2} \frac{r_d^2}{r^2} \right), \\ \kappa_{idz}^2 &= \frac{GM_d}{r^3} \left(1 + \frac{27}{2} \frac{r_d^2}{r^2} \right), \end{aligned} \quad (4)$$

(Binney and Tremaine 1987; hereafter BT, p. 409). Note that $\kappa_{idz}^2 - \Omega_{id}^2 = 9GM_d r_d^2 / r^5$.

The outer, neutral hydrogen disk can be described approximately by a Fermi function for the surface density

$$\Sigma_H = \frac{\Sigma_{H0}}{1 + \exp[k_1(r/R_H - k_2)]} \quad (5)$$

where R_H is the radius inside of which half the neutral hydrogen mass is located, $k_1 \approx 3.70$, and $k_2 \approx 1.21$. This dependence provides a good fit to the data of Broeils and Rhee (1966; their Figure 6a). The total neutral hydrogen mass is $M_H \approx 5.35 R_H^2 \Sigma_{H0}$.

The halo potential is taken to be

$$\Phi_h = \frac{1}{2} v_o^2 \ell n [r_o^2 + r^2 + (z/q)^2], \quad (6a)$$

where $v_o = \text{const.}$ is the circular velocity at large distances, $r_o = \text{const.}$ is the core radius of the halo, and $q = \text{const.}$ is the axial ratio of the equipotential surfaces with $\varepsilon \equiv 1 - q$ their ellipticity. An oblate (prolate) halo corresponds to $q < 1$ ($q > 1$). We have

$$\Omega_h^2 = \frac{v_o^2}{r_o^2 + r^2}, \quad \kappa_{hz}^2 = \frac{(v_o/q)^2}{r_o^2 + r^2}. \quad (6b)$$

The halo is usually assumed to be oblate with $\varepsilon \sim 0.1 - 0.2$ (Nelson and Tremaine 1995). This gives $\kappa_{hz}^2 - \Omega_h^2 = (q^{-2} - 1)\Omega_h^2 \sim (0.23 - 0.56)\Omega_h^2$ which is of interest in the following. For the radii of the warps observed in galaxies ($r \gtrsim 4r_d$), $\kappa_{idz}^2 - \Omega_{id}^2 \ll \Omega_h^2$. For $q = 1$, the halo mass within a radius r is $M_h(r) \approx 0.925 \times 10^{11} M_\odot (r/10\text{kpc})(v_o/200\text{km/s})^2 [r^2/(r^2 + r_o^2)]$.

Perturbations of the galaxy are assumed to consist of small angle tilting ($\theta^2 \ll 1$) of the outer disk with

azimuthal mode number $m = 1$ (or -1). The halo and the inner disk are assumed to be unaffected by the perturbation. We can describe the outer disk by a number N of tilted plane circular rings. This description is *general* for small tilting angles where the linearized equations are applicable. We do not need to assume that the disk is ‘razor thin’ but rather that the disk half-thickness Δz is small, $(\Delta z)^2 \ll r^2$. The vertical displacements of the disk $\sim \theta r$ are in general much larger than Δz .

2.1. One Tilted Ring

The tilting of the ring is completely described by the tilt angle $\theta(t)$, which is the angle between the upward normal to the ring and the z -axis, and the azimuthal angle $\varphi(t)$, which is the angle between the line-of-nodes (where the ring intersects the $z = 0$ plane) and the x -axis. The geometry is shown in Figure 3. The perturbation is assumed to be small in the respect that $\theta^2 \ll 1$. The position vector of a point on the ring is

$$\mathbf{R} = [r \cos \phi, r \sin \phi, h(\phi, t)], \quad 0 \leq \phi \leq 2\pi, \quad (7)$$

(Cartesian components), where $h(\phi, t)$ is the height of the ring above the $z = 0$ plane. We have

$$\begin{aligned} h(\phi, t) &= r\theta(t) \sin[\phi - \varphi(t)], \\ &= r\theta_x(t) \sin \phi - r\theta_y(t) \cos \phi, \end{aligned} \quad (8a)$$

where

$$\theta_x(t) \equiv \theta(t) \cos[\varphi(t)] \quad (8b)$$

is the angle of the tilt about the x -axis, and

$$\theta_y(t) \equiv \theta(t) \sin[\varphi(t)] \quad (8c)$$

is the angle about the y -axis. We have $\theta = \sqrt{\theta_x^2 + \theta_y^2}$ and $\varphi = \tan^{-1}(\theta_y/\theta_x)$.

The angular momentum of the tilted ring is

$$\begin{aligned} \mathbf{L} &= M \int_0^{2\pi} \frac{d\phi}{2\pi} \mathbf{R} \times \frac{d\mathbf{R}}{dt}, \\ &= M\Omega r^2 \hat{\mathbf{z}} + \delta\mathbf{L}, \end{aligned} \quad (9)$$

where $\delta\mathbf{L} = \hat{\mathbf{x}}\delta L_x + \hat{\mathbf{y}}\delta L_y$, M is the ring mass, and Ω is its angular rotation rate which is unaffected by the perturbation to first order in θ . We have

$$\frac{d\mathbf{R}}{dt} = \left. \frac{\partial \mathbf{R}}{\partial s} \right|_t \frac{ds}{dt} + \left. \frac{\partial \mathbf{R}}{\partial t} \right|_s$$

$$= \hat{\mathbf{t}}\Omega r + \left. \frac{\partial \mathbf{R}}{\partial t} \right|_s . \quad (10a)$$

Here, $\hat{\mathbf{t}} = (1/r)(\partial \mathbf{R}/\partial \phi) = [-\sin\phi, \cos\phi, \theta_x \cos\phi + \theta_y \sin\phi]$ is the unit tangent vector to the ring (to first order in θ), s is the distance along the ring circumference measured from, say, the ascending node where $h(\phi, t) = 0$, and

$$\left. \frac{\partial \mathbf{R}}{\partial t} \right|_s = \left[0, 0, r \frac{d\theta_x}{dt} \sin\phi - r \frac{d\theta_y}{dt} \cos\phi \right] . \quad (10b)$$

From equation (9) we have

$$\delta L_x = Mr^2 \left(\Omega \theta_y + \frac{1}{2} \frac{d\theta_x}{dt} \right) , \quad (11a)$$

$$\delta L_y = Mr^2 \left(-\Omega \theta_x + \frac{1}{2} \frac{d\theta_y}{dt} \right) . \quad (11b)$$

The torque on the ring is

$$\mathbf{T} = \int_0^{2\pi} r d\phi \mathbf{R} \times \mathbf{F} , \quad (12a)$$

or

$$T_x = \int_0^{2\pi} r d\phi (r \sin\phi F_z - h F_y) , \quad (12b)$$

$$T_y = - \int_0^{2\pi} r d\phi (r \cos\phi F_z - h F_x) . \quad (12c)$$

The ring is assumed to exert no torque on itself. Consequently, the force \mathbf{F} (per unit circumference) which contributes to \mathbf{T} in equation (12a) is due to the inner disk and the halo. Thus we have

$$F_z = -(M/2\pi r) \bar{\kappa}_z^2 ,$$

where

$$\bar{\kappa}_z^2 \equiv \kappa_{idz}^2 + \kappa_{hz}^2 , \quad (13a)$$

is the vertical epicyclic frequency excluding the contribution due to the outer disk [see equation (3)]. Also,

$$F_x = -(M/2\pi r) \bar{\Omega}^2 r \cos\phi , \quad F_y = -(M/2\pi r) \bar{\Omega}^2 r \sin\phi ,$$

where

$$\bar{\Omega}^2 \equiv \Omega_{id}^2 + \Omega_h^2 , \quad (13b)$$

which excludes the outer disk contribution to Ω^2 [see equation (2)]. Thus we find

$$T_x = -\frac{1}{2} Mr^2 (\bar{\kappa}_z^2 - \bar{\Omega}^2) \theta_x , \quad (14a)$$

$$T_y = -\frac{1}{2} Mr^2 (\bar{\kappa}_z^2 - \bar{\Omega}^2) \theta_y . \quad (14b)$$

The equations of motion $d(\delta \mathbf{L})/dt = \mathbf{T}$ are

$$\frac{d}{dt} \left(I \frac{d\theta_x}{dt} + 2I\Omega \theta_y \right) = -I (\bar{\kappa}_z^2 - \bar{\Omega}^2) \theta_x , \quad (15a)$$

$$\frac{d}{dt} \left(I \frac{d\theta_y}{dt} - 2I\Omega \theta_x \right) = -I (\bar{\kappa}_z^2 - \bar{\Omega}^2) \theta_y , \quad (15b)$$

after multiplying by two and letting $I = Mr^2$ denote the moment of inertia of the ring. The terms of the left-hand side $\propto \Omega$ are due to the Coriolis force.

It is useful to introduce

$$\Theta(t) \equiv \theta_x(t) - i\theta_y(t) = \theta(t) \exp[-i\varphi(t)] . \quad (16)$$

This representation is well-known from treatments of spin precession in quantum mechanics. We can then combine equations (15a) and (15b) to obtain

$$\left(\frac{d^2}{dt^2} + 2i\Omega \frac{d}{dt} \right) \Theta = -\Delta^2 \Theta , \quad (17)$$

where

$$\Delta^2 \equiv \bar{\kappa}_z^2 - \bar{\Omega}^2 . \quad (18)$$

Note that we can have $\Delta^2 < 0$ for a prolate halo. Solutions of equation (17) can be taken as $\Theta = C \exp(-i\omega t)$ with C a complex constant. From equation (17) we have the dispersion relation $(\omega - \Omega)^2 = \Omega^2 + \Delta^2$ which gives

$$\omega = \Omega \pm \sqrt{\Omega^2 + \Delta^2} . \quad (19)$$

In all cases considered here, $\Omega^2 + \Delta^2 > 0$. For $\Omega > 0$, the plus sign corresponds to the *fast mode*, $\omega_2 > 0$, with prograde precession [$\varphi(t)$ increasing], and the minus sign to the *slow mode*, ω_1 , with retrograde precession [$\varphi(t)$ decreasing] (HT). For $|\Delta^2| \ll \Omega^2$ and $\Omega > 0$, the slow mode has $\omega_1 \approx -\Delta^2/(2\Omega)$. These two modes are the analogues of the *normal modes* of vibration of a non-rotating mechanical system. That there are two modes rather than one for each ring is due to the Doppler splitting from the rotation (Ω).

A general solution of equation (17) is

$$\Theta(t) = C_1 \exp(-i\omega_1 t) + C_2 \exp(-i\omega_2 t) , \quad (20)$$

where ω_1 and ω_2 are the two roots given in equation (19), and C_1 and C_2 are complex constants. The four real quantities determine the initial values $\theta_x(0)$, $\theta_y(0)$, $d\theta_x(0)/dt$, and $d\theta_y(0)/dt$. If only the fast or

slow mode is excited (C_1 or $C_2 = 0$), then $\theta = \text{Const.}$ and $\varphi = \omega_\alpha t + \text{Const.}'$ with $\alpha = 1, 2$. A simple way to excite only the slow or fast mode is to take $\theta_x(0) = C_\alpha$, $\theta_y(0) = 0$, $d\theta_x(0)/dt = 0$, and $d\theta_y(0)/dt = \omega_\alpha C_\alpha$. Figure 4 illustrates the two limiting cases of $C_1/C_2 \ll 1$ and $C_1/C_2 \gg 1$.

We can recast equations (15) in a form equivalent to that given by HT by multiplying equation (15a) by $\sin\phi$ and equation (15b) by $\cos\phi$ and subtracting the two. Noting that $\partial h/\partial\phi = r\theta_x\cos\phi + r\theta_y\sin\phi$ and $\partial^2 h/\partial\phi^2 = -h$, we obtain

$$\left(\frac{\partial}{\partial t} + \Omega \frac{\partial}{\partial\phi}\right)^2 h = -\left(\bar{\kappa}_z^2 + \Omega^2 - \bar{\Omega}^2\right) h.$$

Note that $h(r, \phi, t)$ is non-zero only for r equal to the ring radius. From equation (2) we have

$$\Omega^2 - \bar{\Omega}^2 = \frac{1}{r} \frac{\partial\Phi_{ring}}{\partial r}.$$

For a toroidal ring of minor radius $\Delta r \ll r$, this difference is of the order of $GM\ell n(r/\Delta r)/r^3$. In the absence of a halo, the right hand side of the equation for h is

$$-(\kappa_{idz}^2 + \Omega^2 - \bar{\Omega}^2)h,$$

which is the same as the HT expression

$$-G \int d^2 r' \frac{\Sigma(r') [h(r, \phi, t) - h(r', \phi', t)]}{|\mathbf{r} - \mathbf{r}'|^3}.$$

The κ_{idz}^2 term comes from the integration of over $r' < r$ while the $\Omega^2 - \bar{\Omega}^2$ term is from the integration over $r' \approx r$.

Multiplying equation (15a) by $d\theta_x/dt$ and (15b) by $d\theta_y/dt$ and adding the two gives $d\mathcal{E}_{ring}/dt = 0$, where the energy of the tilted ring is

$$\mathcal{E}_{ring} = \frac{1}{2}I \left(\dot{\theta}_x^2 + \dot{\theta}_y^2\right)^2 + \frac{1}{2}I\Delta^2 (\theta_x^2 + \theta_y^2) = \text{Const.}, \quad (21)$$

where a dot denotes a time derivative. This expression agrees with the result of HT (their Appendix B). In the absence of a halo or with an oblate halo ($\kappa_{hz}^2 > \Omega_h^2$), we have $\Delta^2 > 0$, so that both terms in \mathcal{E}_{ring} are non-negative which implies stability of the ring tilting. In the case of a prolate halo with $\Delta^2 < 0$ instability is possible.

In order to understand the stability of the ring tilting, it is useful to consider the influence of a small Newtonian drag or friction on the ring motion, a force

$\mathbf{F}^f = -(M/2\pi r)\beta\partial\mathbf{R}/\partial t|_s$ per unit circumference, with $\beta > 0$ but $\beta^2 \ll \Omega^2$. This drag could result from dynamical friction of the ring with the dark halo matter (Nelson and Tremaine 1995).

The full calculation of β due to dynamical friction on a precessing ring is complicated (Nelson and Tremaine 1995), but an estimate based on treating the ring as two point masses $M/2$ at the points $\max|h|$ (Weinberg 1985) gives

$$\begin{aligned} \beta/\Omega &\sim 2fGM\ell n\Lambda/(3\sqrt{\pi}v_o^2r) \\ &\approx 0.035\ell n\Lambda \left(\frac{M}{10^{10}M_\odot}\right) \left(\frac{200\text{km/s}}{v_o}\right)^2 \left(\frac{10\text{kpc}}{r}\right), \end{aligned} \quad (22)$$

where $\ell n\Lambda = \mathcal{O}(3)$ is the Coulomb logarithm, v_o is the circular velocity, and $f = r^2(r^2 + 3r_o^2)/(r^2 + r_o^2)^2$ accounts for the density profile of the halo, with r_o the halo core radius. Later, in §3, where we represent the outer disk as N tilted interacting rings, the pertinent estimate for β_j for a single ring is this formula with M the total mass of the outer disk rather than the mass of a single ring (Weinberg 1985).

The drag torque due to \mathbf{F}^f is $T_x^f = -\frac{1}{2}Mr^2\beta(d\theta_x/dt)$ and $T_y^f = -\frac{1}{2}Mr^2\beta(d\theta_y/dt)$. Solution of equation (17) including \mathbf{T}^f gives

$$\omega = \Omega \pm \sqrt{\Omega^2 + \Delta^2} - \frac{i\beta}{2} \left(1 \pm \frac{\Omega}{\sqrt{\Omega^2 + \Delta^2}}\right). \quad (23)$$

Thus, both fast and slow precession modes with $\Delta^2 > 0$ are stable in the presence of friction, whereas the slow precession mode with $\Delta^2 < 0$ is unstable [$\omega_i \equiv \text{Im}(\omega) > 0$]. For the slow precession mode, the kinetic energy term $\propto \dot{\theta}_{x,y}^2$ in \mathcal{E}_{ring} is smaller than the magnitude of the potential energy term $\propto \theta_{x,y}^2$ for $|\Delta^2| < \Omega^2$. In the presence of the friction force, $d\mathcal{E}_{ring}/dt = -I\beta(\dot{\theta}_x^2 + \dot{\theta}_y^2)$. Thus, for the slow precession mode, $\mathcal{E}_{ring} \propto \Delta^2$ is negative if $\Delta^2 < 0$, and the tilt angle grows. The instability is therefore a *negative energy dissipative* instability. An analogous instability was predicted and observed for the precession of laboratory collisionless relativistic electron rings (Furth 1965; Beal et al. 1969). The instability also occurs in the presence of a non-Newtonian (nonlinear) friction force on the ring.

A second quadratic integral of the motion of equations (15), analogous to angular momentum (see following), can be obtained by multiplying equation (15a) by $-\theta_y$ and equation (15b) by θ_x and adding.

This gives $d\mathcal{P}_{ring}/dt = 0$, where

$$\begin{aligned}\mathcal{P}_{ring} &= I \left(\dot{\theta}_y \dot{\theta}_x - \dot{\theta}_x \dot{\theta}_y \right) + I\Omega \left(\theta_x^2 + \theta_y^2 \right), \\ &= I\theta^2 (\Omega - \dot{\varphi}) = \text{Const.}\end{aligned}\quad (24)$$

An analogous constant of the motion exists for cases of two or more rings (see §§2.3, 3, and 4). This constant of the motion is a new result of the present work. For the case of instability, with ω complex, $d\phi/dt = \omega_r \equiv \text{Re}(\omega)$. With the above-mentioned friction force included, we have $d\mathcal{P}_{ring}/dt = \beta I\theta^2 \omega_r$, which is compatible with equation (23) which shows instability for $\Delta^2 < 0$ and gives $0 < \omega_r < \Omega$ and $\mathcal{P}_{rings} > 0$.

The second integral (24) can be understood by noting that equations (15) follow from the Lagrangian

$$\begin{aligned}\mathcal{L} &= \frac{1}{2}I \left(\dot{\theta}_x^2 + \dot{\theta}_y^2 \right) + I\Omega \left(\theta_y \dot{\theta}_x - \theta_x \dot{\theta}_y \right) \\ &\quad - \frac{1}{2}I\Delta^2 \left(\theta_x^2 + \theta_y^2 \right).\end{aligned}\quad (25a)$$

A canonical transformation to the variables θ and φ gives

$$\mathcal{L} = \frac{1}{2}I \left(\dot{\theta}^2 + \theta^2 \dot{\varphi}^2 \right) - I\Omega\theta^2 \dot{\varphi} - \frac{1}{2}I\Delta^2\theta^2.\quad (25b)$$

Thus the canonical momentum $P_\varphi = \partial\mathcal{L}/\partial\dot{\varphi} = I\theta^2 (\dot{\varphi} - \Omega) = \text{Const.} = -\mathcal{P}_{rings}$ because $\partial\mathcal{L}/\partial\varphi = 0$. On the other hand, $P_\theta = I\dot{\theta}$ depends on time. The Hamiltonian $\mathcal{H}(\theta, \varphi, P_\theta, P_\varphi) = \theta(\partial\mathcal{L}/\partial\dot{\theta}) + \dot{\varphi}(\partial\mathcal{L}/\partial\dot{\varphi}) - \mathcal{L}$ is

$$\mathcal{H} = \frac{P_\theta^2}{2I} + \frac{1}{2I} \left(\frac{P_\varphi}{\theta} + I\Omega\theta \right)^2 + \frac{1}{2}I\Delta^2\theta^2,\quad (25c)$$

and $\mathcal{H} = \mathcal{E}_{ring} = \text{Const.}$ in that \mathcal{L} has no explicit time dependence.

The θ -dependent terms of \mathcal{H} can evidently be viewed as an effective potential for the θ motion. In general (for $P_\varphi \neq 0$), θ nutates between a minimum and a maximum value. The angular frequency of the nutation is $2(\Omega^2 + \Delta^2)^{\frac{1}{2}}$ so that the *nutations period* is $P_{nut} = (P/2)(1 + \Delta^2/\Omega^2)^{-\frac{1}{2}}$, where $P = 2\pi/\Omega$ is the period of the orbit. This can also be seen by noting that with $\Theta(t)$ given in general by equation (20), we have $|\Theta(t)| = |C_1 + C_2 \exp[-i(\omega_2 - \omega_1)t]|$ and $\omega_2 - \omega_1 = 2(\Omega^2 + \Delta^2)^{\frac{1}{2}}$. For $|\Delta^2|/\Omega^2 \equiv \epsilon \ll 1$, the period of the slow mode $P_1 = 2\pi/|\omega_1| \approx (2/\epsilon)P \gg P_{nut}$, while the fast mode period $P_2 = 2\pi/\omega_2 \approx (P/2)(1 - \epsilon/4)$

is slightly longer than the nutation period $P_{nut} \approx (P/2)(1 - \epsilon/2)$. The nutation of the ring is clearly evident in Figure 4. For $|C_1/C_2| < 1$ (Figure 4a), $\Theta(t)$ nutates many ($\approx 4/\epsilon$) times in the period P_1 of motion of Θ about the origin. On the other hand, for $|C_1/C_2| > 1$ (Figure 4b), $\Theta(t)$ has an elliptical path with the azimuth of say the maximum of $|\Theta(t)|$ precessing slowly in the clockwise direction with a period $\approx (2/\epsilon)P$.

A counter-rotating ring with $\Omega \rightarrow -\Omega$ behaves in the same way as a co-rotating ring. For $\Delta^2 > 0$, the ring slow mode precession is retrograde relative to the ring particle motion but of course prograde relative to our coordinate system.

2.2. Interpretation of Ring Observations

Warps of spiral galaxies are deduced from measurements of 21 cm line neutral hydrogen emission. Here, we consider the spectral signature of a single ring in either the slow precession mode or the fast precession mode. The observer is considered to be in the (x, z) plane at an angle ψ to the z -axis. The velocity of the ring matter is given by equation (10). Thus, the velocity of the HI in the direction of the observer is

$$\begin{aligned}v_{\parallel}(\phi)/(r\Omega) &= -\sin(\psi)\sin(\phi) \\ &\quad + \theta \left(1 - \frac{\omega_\alpha}{\Omega} \right) \cos(\psi)\cos(\phi - \varphi).\end{aligned}\quad (26)$$

The spectrum of the ring is $\mathcal{S}(v_{\parallel}) \propto |dv_{\parallel}/d\phi|^{-1} \propto (1 - v_{\parallel}^2/v_{\parallel\text{max}}^2)^{-\frac{1}{2}}$. The ring motion $\partial\mathbf{R}/\partial t|_s$ enters through the term involving ω_α . For a ring in the slow precession mode with $|\omega_1/\Omega| \ll 1$, the ring motion has only a small affect on $v_{\parallel}(\phi)$. The situation is very different for a ring in the fast precession mode where $\omega_2/\Omega > 2$ if $\Delta^2 > 0$. In this case the sign of the term in $v_{\parallel}(\phi)$ proportional to θ is reversed which corresponds to a change of the line-of-nodes angle φ by $\pm 180^\circ$. Observations are interpreted assuming negligible ring motion, $|\omega_\alpha/\Omega| \ll 1$, and this is wrong if the fast precession mode(s) is excited. The fast precession modes of a system with many rings may disappear from view over a long enough time due to phase-mixing (see §3.1 and §3.2).

2.3. Two Tilted Rings

Consider now the case of two tilted plane circular rings of mass M_j and angular rotation rate Ω_j at radii

r_j with $j = 1, 2$. We have

$$\delta L_{jx} = +\frac{1}{2}I_j \frac{d\theta_{jx}}{dt} + I_j \Omega_j \theta_{jy}, \quad (27a)$$

$$\delta L_{jy} = +\frac{1}{2}I_j \frac{d\theta_{jy}}{dt} - I_j \Omega_j \theta_{jx}, \quad (27b)$$

where θ_{jx} and θ_{jy} are the tilt angles and $I_j \equiv M_j r_j^2$ the moments of inertia for the two rings.

To obtain the torque on, say, ring 1, we exclude as before the force due to this ring on itself. Thus the horizontal force on ring 1 is

$$(\mathbf{F}_1)_{x,y} = -M_1 \left(\Omega_{id}^2 + \Omega_h^2 + \frac{1}{r} \frac{\partial \Phi_{R2}}{\partial r} \right)_1 (x_1, y_1), \quad (28)$$

where the Φ_{R2} is the gravitational potential due to ring 2, and the 1-subscript on the parenthesis indicates evaluation at $r = r_1$. Note that

$$\begin{aligned} \left(\frac{1}{r} \frac{\partial \Phi_{R2}}{\partial r} \right)_1 &= \frac{1}{r_1} \frac{\partial}{\partial r_1} \int_0^{2\pi} \frac{d\phi}{2\pi} \frac{GM_2}{|\mathbf{r}_1 - \mathbf{r}_2|} \\ &= GM_2 I_{12} - GM_2 r_2 J_{12} / r_1, \end{aligned} \quad (29)$$

where

$$I_{12} \equiv \int_0^{2\pi} \frac{d\phi}{2\pi} \frac{1}{(r_1^2 + r_2^2 - 2r_1 r_2 \cos\phi)^{\frac{3}{2}}}, \quad (30a)$$

$$J_{12} \equiv \int_0^{2\pi} \frac{d\phi}{2\pi} \frac{\cos\phi}{(r_1^2 + r_2^2 - 2r_1 r_2 \cos\phi)^{\frac{3}{2}}}. \quad (30b)$$

There is also the vertical force on ring 1,

$$F_{1z} = -(M_1/2\pi r_1) (\kappa_{idz}^2 + \kappa_{hz}^2)_1 h_1 + F_z^{12}, \quad (31a)$$

where

$$F_z^{12} = - \int_0^{2\pi} \frac{d\phi'}{2\pi} \frac{GM_1 M_2 [h_1(\phi, t) - h_2(\phi', t)]}{[r_1^2 + r_2^2 - 2r_1 r_2 \cos(\phi - \phi')]^{\frac{3}{2}}} \quad (31b)$$

is the vertical force on ring 1 due to ring 2. This integral can be simplified by noting that

$$\begin{aligned} h_2(\phi', t) &= r_2 \theta_2 \sin(\phi - \varphi_2 + \phi' - \phi) \\ &= h_2 \cos(\phi' - \phi) - r_2 \theta_2 \cos(\phi - \varphi_2) \sin(\phi' - \phi). \end{aligned} \quad (31c)$$

The $\sin(\phi - \phi')$ term in equation (31c) does not contribute to the integral (31b). Thus we have

$$\int_0^{2\pi} r_1 d\phi \mathbf{R}_1 \times (\hat{\mathbf{z}} F_z^{12}) =$$

$$\begin{aligned} & -\frac{1}{2} GM_1 M_2 r_1^2 I_{12} \theta_{1x} \hat{\mathbf{x}} + \frac{1}{2} GM_1 M_2 r_1 r_2 J_{12} \theta_{2x} \hat{\mathbf{x}} \\ & -\frac{1}{2} GM_1 M_2 r_1^2 I_{12} \theta_{1y} \hat{\mathbf{y}} + \frac{1}{2} GM_1 M_2 r_1 r_2 J_{12} \theta_{2y} \hat{\mathbf{y}}. \end{aligned} \quad (32)$$

Combining terms in equations (12b) and (12c) gives

$$T_{1x} = -\frac{1}{2} M_1 r_1^2 \Delta_1^2 \theta_{1x} - \frac{1}{2} C_{12} (\theta_{1x} - \theta_{2x}), \quad (33a)$$

$$T_{1y} = -\frac{1}{2} M_1 r_1^2 \Delta_1^2 \theta_{1y} - \frac{1}{2} C_{12} (\theta_{1y} - \theta_{2y}), \quad (33b)$$

where

$$C_{12} \equiv GM_1 M_2 r_1 r_2 J_{12} \quad (34)$$

measures the strength of the gravitational interaction between the two rings, and Δ^2 is defined in equation (18). The two terms involving the integral I_{12} cancel. Note that C_{12} is symmetric between the two rings and that it is non-negative because $J_{12} \geq 0$ [see equation (45e) and Figure 5].

The torque on ring 2 is found in the same way to be

$$T_{2x} = -\frac{1}{2} M_2 r_2^2 \Delta_2^2 \theta_{2x} - \frac{1}{2} C_{12} (\theta_{2x} - \theta_{1x}), \quad (35a)$$

$$T_{2y} = -\frac{1}{2} M_2 r_2^2 \Delta_2^2 \theta_{2y} - \frac{1}{2} C_{12} (\theta_{2y} - \theta_{1y}). \quad (35b)$$

The equations of motion are

$$d(\delta \mathbf{L}_1)/dt = \mathbf{T}_1, \quad d(\delta \mathbf{L}_2)/dt = \mathbf{T}_2. \quad (36)$$

For the limit where the only torques are those due to the two rings, $\Delta_1^2 = 0$ and $\Delta_2^2 = 0$, we find

$$\frac{d}{dt} (\delta \mathbf{L}_1 + \delta \mathbf{L}_2) = 0, \quad (37)$$

which is a necessary result.

We can follow the steps leading to equation (22) to obtain $d\mathcal{E}_{rings}/dt = 0$ for the energy \mathcal{E}_{rings} of the two tilted rings, where

$$\begin{aligned} \mathcal{E}_{rings} &= \frac{1}{2} \sum_{j=1}^2 I_j (\dot{\theta}_{jx}^2 + \dot{\theta}_{jy}^2) + \frac{1}{2} \sum_{j=1}^2 I_j \Delta_j^2 (\theta_{jx}^2 + \theta_{jy}^2) \\ &+ \frac{1}{2} C_{12} (\theta_{1x} - \theta_{2x})^2 + \frac{1}{2} C_{12} (\theta_{1y} - \theta_{2y})^2, \end{aligned} \quad (38)$$

where $I_1 \equiv M_1 r_1^2$ and $I_2 \equiv M_2 r_2^2$ are the moments of inertia of the two rings. This energy is non-negative and the rings are stable if both Δ_1^2 and Δ_2^2 are non-negative. Also, in this case the rings are stable in the presence of dissipative forces such as the friction

force of Subsection 2.1. Thus a necessary condition for instability with or without dissipation is that Δ_1^2 and/or Δ_2^2 be negative.

A second quadratic integral of the motion can be obtained by following the steps leading to equation (24). We find $d\mathcal{P}_{rings}/dt = 0$, where

$$\mathcal{P}_{rings} = I_1\theta_1^2 (\Omega_1 - \dot{\varphi}_1) + I_2\theta_2^2 (\Omega_2 - \dot{\varphi}_2) . \quad (39)$$

For the case of instability, $\omega = \omega_r + i\omega_i$, $\omega_i > 0$, we have $d\varphi_j/dt = \omega_r$. Thus, a further necessary condition for instability in the absence of dissipation (in addition to Δ_1^2 and/or Δ_2^2 being negative) is that $\Omega_1 - \omega_r$ and $\Omega_2 - \omega_r$ have different signs; that is, $\Omega_2 < \omega_r < \Omega_1$ for $\Omega_2 < \Omega_1$. For the slow precession modes with $|\omega_r| \ll \Omega_j$, this corresponds to counter-rotating rings, $\Omega_1/\Omega_2 < 0$.

The Lagrangian for the two ring system is

$$\begin{aligned} \mathcal{L} = & \frac{1}{2} \sum_{j=1}^2 I_j \left(\dot{\theta}_j^2 + \theta_j^2 \dot{\varphi}_j^2 - 2\Omega_j \theta_j^2 \dot{\varphi}_j - \Delta_j^2 \theta_j^2 \right) - \\ & \frac{1}{2} C_{12} \left[\theta_1^2 + \theta_2^2 - 2\theta_1\theta_2 \cos(\varphi_1 - \varphi_2) \right] . \end{aligned} \quad (40)$$

The corresponding Hamiltonian $\mathcal{H} = \sum (\dot{\theta}_j \partial \mathcal{L} / \partial \dot{\theta}_j + \dot{\varphi}_j \partial \mathcal{L} / \partial \dot{\varphi}_j) - \mathcal{L}$ is equal in value to \mathcal{E}_{rings} of equation (38). The second constant of the motion, $\mathcal{P}_{rings} = -P_{\varphi_1} - P_{\varphi_2}$, where $P_{\varphi_j} \equiv \partial \mathcal{L} / \partial \dot{\varphi}_j$. Note that $dP_{\varphi_1}/dt = \partial \mathcal{L} / \partial \varphi_1 = -\frac{1}{2} \theta_1 \theta_2 \sin(\varphi_1 - \varphi_2)$ and that $dP_{\varphi_2}/dt = \partial \mathcal{L} / \partial \varphi_2 = \frac{1}{2} \theta_1 \theta_2 \sin(\varphi_1 - \varphi_2)$ so that $d(P_{\varphi_1} + P_{\varphi_2})/dt = 0$.

As in the case of a single ring, it is useful to introduce

$$\Theta_1(t) \equiv \theta_{1x} - i\theta_{1y} = \theta_1(t) \exp[-i\varphi_1(t)] , \quad (41a)$$

$$\Theta_2(t) \equiv \theta_{2x} - i\theta_{2y} = \theta_2(t) \exp[-i\varphi_2(t)] . \quad (41b)$$

The equations of motion (36) can then be written as

$$\left(\frac{d^2}{dt^2} + 2i\Omega_1 \frac{d}{dt} \right) \Theta_1 = -\Delta_1^2 \Theta_1 - \frac{C_{12}}{I_1} (\Theta_1 - \Theta_2) , \quad (42a)$$

$$\left(\frac{d^2}{dt^2} + 2i\Omega_2 \frac{d}{dt} \right) \Theta_2 = -\Delta_2^2 \Theta_2 - \frac{C_{12}}{I_2} (\Theta_2 - \Theta_1) , \quad (42b)$$

after dividing through by $I_j/2$.

For Θ_1 and $\Theta_2 \propto \exp(-i\omega t)$, we get the dispersion relation

$$\left[(\omega - \Omega_1)^2 - K_1^2 \right] \left[(\omega - \Omega_2)^2 - K_2^2 \right] = \frac{C_{12}^2}{I_1 I_2} , \quad (43)$$

where

$$K_j^2 \equiv \Omega_j^2 + \Delta_j^2 + \frac{C_{12}}{I_j} ,$$

with $j = 1, 2$. Equation (43) can readily be solved for the four roots. Two of these roots are high-frequency, *fast precession modes* with $\omega \geq 2\Omega_j$, assuming $\Omega_j > 0$ and $\Delta_j^2 \geq 0$. The other two roots are the *slow precession modes* with much smaller frequencies, typically, $\omega^2 \ll \Omega_j^2$.

In order to get simple analytic results, we first consider the low-frequency modes $\omega^2 \ll \Omega_j^2$, assuming $|\Delta_j^2| \ll \Omega_j^2$ and $C_{12}/I_j \ll \Omega_j^2$. We can then neglect the second time derivatives in equations (42) and the ω^2 terms in equation (43), and this leads to a quadratic dispersion equation for ω . The roots of this equation are

$$\begin{aligned} \omega = & \frac{1}{2} [\omega_{p1} + \omega_{p2} - \omega_{g12} (1 + \ell_{12})] \\ & \pm \frac{1}{2} \left\{ [\omega_{p2} - \omega_{p1} + \omega_{g12} (1 - \ell_{12})]^2 + 4\omega_{g12}^2 \ell_{12} \right\}^{\frac{1}{2}} . \end{aligned} \quad (44)$$

Here,

$$\omega_{pj} \equiv -\frac{\Delta_j^2}{2\Omega_j} , \quad (45a)$$

for $j = 1, 2$, are the slow precession frequencies of the two rings in the absence of gravitational interaction between them ($C_{12} = 0$);

$$\omega_{g12} \equiv \frac{C_{12}}{2L_1} \quad \text{and} \quad \ell_{12} \equiv \frac{L_1}{L_2} , \quad (45b)$$

where ω_{g12} is a frequency which measures the strength of the gravitational interaction between the two rings, and where $L_j \equiv I_j \Omega_j$ are the angular momenta of the two rings. We have

$$\begin{aligned} \frac{\omega_{g12}}{\Omega_1} \approx & 2.8 \times 10^{-2} \left(\frac{M_2}{10^{10} M_\odot} \right) \times \\ & \left(\frac{20 \text{ kpc}}{r_2} \right) \left(\frac{200 \text{ km/s}}{\Omega_1 r_1} \right)^2 J'_{12} , \end{aligned} \quad (45c)$$

where

$$J'_{12} \equiv \delta \int_0^{2\pi} \frac{d\phi}{2\pi} \frac{\cos\phi}{[1 + \delta^2 - 2\delta\cos\phi]^{\frac{3}{2}}} , \quad (45e)$$

with $\delta = r_1/r_2 \leq 1$. For $\delta \ll 1$, $J'_{12} \rightarrow \frac{3}{2}\delta^2$. For $1 - \delta \ll 1$, $J'_{12} \rightarrow 1/[\pi(1 - \delta)^2]$. We assume that $1 - \delta > \Delta z/r$, where Δz is the disk thickness. The dependence of J'_{12} on δ is shown in Figure 5.

A simple limit of equation (44) is that where $\Delta_1^2 = 0 = \Delta_2^2$. The two roots are then $\omega = 0$ and $\omega = -\omega_{g12}(1 + \ell_{12}) = -\frac{1}{2}C_{12}L_1L_2/(L_1 + L_2)$. The zero frequency mode corresponds to both rings tilted by the same angle, $\Theta_1 = \Theta_2$, which is the rigid tilt mode (HT). The other mode has $\Theta_1 = -(L_2/L_1)\Theta_2$; that is, the rings are tilted in opposite directions for $L_1/L_2 > 0$.

We first consider co-rotating rings where the four ω roots of equation (43) are real in the absence of dissipation. Note that the low frequency roots of equation (44) are real for $\ell_{12} > 0$. A general solution for the motion of the two rings is then

$$\Theta_j = \sum_{\alpha=1}^4 C_{j\alpha} \exp(-i\omega_\alpha t), \quad (46)$$

where $\{\omega_\alpha\}$ are the four mentioned frequencies, and $\{C_{j\alpha}\}$ are 8 complex constants. However, only 8 real quantities are needed to specify general initial conditions because the $\{C_{1\alpha}\}$ are related to the $\{C_{2\alpha}\}$ by equations (42). If only a *single* mode of the system is excited, then $\Theta_1 = C_{1\beta}\exp(-i\omega_\beta t)$ and $\Theta_2 = C_{2\beta}\exp(-i\omega_\beta t)$. Equations (42) then imply that Θ_2/Θ_1 is real. Because $\Theta_j = \theta_j\exp(-i\varphi_j)$, we conclude that $\Theta_2/\Theta_1 \propto \exp[-i(\varphi_2 - \varphi_1)]$ is real so that $\varphi_2 - \varphi_1$ is either 0 or π . That is, the rings are either tilted in the same direction and precess together or they are tilted in opposite directions and also precess together. From equations (42), $\Theta_2/\Theta_1 = I_1 [K_1^2 - (\omega_\beta - \Omega_1)^2] / C_{12}$.

Figure 6a shows the ω_{g12} dependence of the frequencies of the two slow-precession modes obtained from equations (43) and (44) for the case where both rings are co-rotating and the halo is *oblate*. The ‘slower’ of the two modes has $\Theta_2/\Theta_1 > 0$, while the other has $\Theta_2/\Theta_1 < 0$ as shown in Figure 6b. The larger gravitational torque in the second case accounts for the faster retrograde precession. As ω_{g12} increases, the frequency of the slower mode approaches

$$\omega_1 \rightarrow \frac{L_1\omega_{p1}}{L_1 + L_2} + \frac{L_2\omega_{p2}}{L_1 + L_2}. \quad (47)$$

and $\Theta_2/\Theta_1 \rightarrow 1$ for $\omega_{g12} \gg |\omega_{p2} - \omega_{p1}|/(1 + \ell_{12})$, where the ω_{pj} are defined in equation (45a). This result can be derived from equation (43) or (44). For the case of N rings and sufficiently large ω_{gjk} , we find in general that the lowest frequency approaches the angular momentum weighted average of the single ring precession frequencies ω_{pj} [equation (45a)].

In contrast with the dependence of ω_1 , ω_2 decreases monotonically as ω_{g12} increases.

From the approximate equation (44) for the slow precession modes, we can distinguish *weak* and *strong-coupling* limits of two co-rotating rings. The coupling strength is measured by the dimensionless parameter

$$\xi_{12} \equiv \frac{\omega_{g12}(1 + \ell_{12})}{|\omega_{p2} - \omega_{p1}|} = \frac{GJ_{12}(L_1 + L_2)}{2(\Omega_1 r_1)(\Omega_2 r_2)|\omega_{p2} - \omega_{p1}|}, \quad (48)$$

which is symmetrical in the ring indices (unlike ω_{g12}). For *weak coupling*, $\xi_{12} \ll 1$, the two rings are affected little by their gravitational interaction, and the two slow mode frequencies are $\omega_1 \approx \omega_{p2}$ with $\Theta_2/\Theta_1 \gg 1$ and $\omega_2 \approx \omega_{p1}$ with $|\Theta_1/\Theta_2| \gg 1$. In the opposite limit of *strong coupling*, $\xi_{12} \gg 1$, the gravitational interaction of the two rings is important, and ω_1 is given approximately by equation (47) with $\Theta_2/\Theta_1 \sim 1$, and $|\omega_2| \gg |\omega_1|$ with $\Theta_2/\Theta_1 < 0$.

For nearby rings, $(\Delta r)^2 = (r_2 - r_1)^2 \ll r_2^2$, of equal mass $M_1 = M_2 = 2\pi r \Delta r \Sigma$ (with Σ the surface mass density of the disk at r), we have $J_{12} \approx 1/[\pi r (\Delta r)^2]$, $|\omega_{p2} - \omega_{p1}| \approx |\partial\omega_p/\partial r|\Delta r$, and thus

$$\xi_{12} \approx \frac{2G\Sigma}{\Omega(\Delta r)^2 |\partial\omega_p/\partial r|}. \quad (49)$$

Evidently, there is strong (weak) coupling for $\Delta r \ll \Delta r_c$ ($\Delta r \gg \Delta r_c$), where Δr_c corresponds to $\xi_{12} = 1$ so that

$$\Delta r_c = \left[\frac{2G\Sigma}{\Omega |\partial\omega_p/\partial r|} \right]^{\frac{1}{2}}. \quad (50a)$$

Assuming a flat rotation curve ($\Omega r = \text{const.}$) and $(\Delta/\Omega)^2 = \text{const.}$, we obtain

$$\Delta r_c \approx 13.2 \text{ kpc} \left(\frac{200 \text{ km/s}}{\Omega r} \right) \left(\frac{r}{20 \text{ kpc}} \right)^{\frac{3}{2}} \times \left(\frac{0.2}{|\Delta^2/\Omega^2|} \right)^{\frac{1}{2}} \left(\frac{\Sigma}{10 \text{ M}_\odot/\text{pc}^2} \right)^{\frac{1}{2}}. \quad (50b)$$

Rings closer together than Δr_c will be strongly coupled.

Figure 7 shows sample orbits of Θ_1 and Θ_2 for two co-rotating rings in an oblate halo for initial conditions $\Theta_1/\Theta_2 = 1/2$ and $\dot{\Theta}_1 = 0 = \dot{\Theta}_2$. The top panel shows a case of weak coupling (small ξ_{12}) where the line-of-nodes φ_j of the two rings regress essentially

independently with the result that $\varphi_2 - \varphi_1$ increases linearly with time. The bottom panel is for a case of strong coupling (large ξ_{12}) where the line-of-nodes are *phase-locked* in the sense that the time average of $\varphi_2 - \varphi_1$ is zero. Figure 8 shows the azimuthal angle difference of the line-of-nodes for the two cases of Figure 7. In the case of weak coupling, a low frequency initial perturbation excites both low frequency modes which have similar frequencies ($\omega_2 \sim 2\omega_1$), and this gives the unlocked behavior. For strong coupling, the initial perturbation excites mainly the ω_1 mode because $|\omega_2| \gg |\omega_1|$, and this gives the locked behavior. For the parameters of figures 4 and 5, note that $\xi_{12} \approx 60\omega_{g12}/\Omega_1$.

Figure 9a shows the ω_{g12} dependence of the frequencies of the two slow-precession modes obtained from equation (43) for the case where both rings are co-rotating and the halo is *prolate*. (We have adopted the convention of ordering the mode frequencies by their magnitudes for $\omega_{g12} \rightarrow 0$.) Figure 9b shows that the ω_2 mode has $\Theta_2/\Theta_1 > 0$. As in the case of an oblate halo, for large ω_{g12} or ξ_{12} , ω_2 approaches the limit given by equation (47) and $\Theta_2/\Theta_1 \rightarrow 1$.

As in the case of a single ring in a prolate halo potential [see equation (23)], small friction torques, with friction coefficients β_1 and β_2 , on two co-rotating rings in a prolate halo lead to a negative energy dissipative instability. We find that the slow modes with prograde precession, $\omega_\alpha > 0$, are unstable in the presence of dissipation. That is, the ω_1 mode in Figure 9 is unstable (stable) for $\omega_{g12} < (>) 0.02$, whereas the ω_2 mode is unstable for all ω_{g12} . The two high frequency modes are prograde but are damped by friction for all ω_{g12} . As in the case of an oblate halo (Figure 8), we observe phase-locking for sufficiently large values of ξ_{12} .

Frictional torques between two co-rotating rings in a prolate halo also give rise to a negative energy dissipative instability. Such torques could arise from the viscous interaction between adjacent gaseous rings. These frictional torques do not change the total angular momentum of the two rings. Therefore, these frictional torques, if Newtonian (linear) in nature, are *necessarily* of the form that they contribute terms

$$-\left(\frac{I_2}{I_1}\right)^{\frac{1}{2}} \beta_{12} (\dot{\Theta}_1 - \dot{\Theta}_2) , \quad (51a)$$

$$-\left(\frac{I_1}{I_2}\right)^{\frac{1}{2}} \beta_{12} (\dot{\Theta}_2 - \dot{\Theta}_1) , \quad (51b)$$

on the right hand sides of equations (42a) and (42b), respectively, where β_{12} is the friction coefficient (with units of angular frequency). For a gas with kinematic shear viscosity ν (with units of cm^2/s) the terms (51) arise from the momentum flux density or stress T_{rz} due to the different vertical velocities of the two rings as a function of ϕ . This gives $\beta_{12} = \nu/(\Delta r)^2$, where $\Delta r = r_2 - r_1$. The relevant viscosity is that due to turbulence in the gas $\nu = \nu_t$ owing to the smallness of the microscopic viscosity. An estimate of ν_t can be made following the proposal of Shakura (1973) and Shakura and Sunyaev (1973) that $\nu_t = \alpha c_s \Delta z$, where c_s is the sound speed, Δz is the half-thickness of the disk, and α is a dimensionless constant thought to be in the range 10^{-3} to 1. In Sections 3 and 4 we discuss further the frictional torques between adjacent rings.

2.4. Two Tilted, Counter-Rotating Rings

Here, we consider the case of two tilted rings which are rotating in opposite directions. This situation is pertinent to observed counter-rotating galaxies (see, for example, Jore, Broeils, and Haynes 1996). From equation (44), instability is possible (in the absence of dissipation) only for $\ell_{12} < 0$ in agreement with our discussion of equation (39). Thus, consider ring 2 to be counter-rotating ($\Omega_2 < 0$ and $L_2 < 0$), while ring 1 is co-rotating. The region of instability is bounded by the two curves

$$\begin{aligned} \omega_{p2} - \omega_{p1} &= \frac{\Delta_1^2}{2|\Omega_1|} + \frac{\Delta_2^2}{2|\Omega_2|} \\ &= \left(-1 \pm 2|\ell_{12}|^{\frac{1}{2}} - |\ell_{12}|\right) \omega_{g12} , \end{aligned} \quad (52)$$

on which the square root in equation (44) is zero. The curves are shown in Figure 10. For parameters in the region between the two curves there is instability, which is seen to occur only for Δ_1^2 and/or Δ_2^2 negative. For fixed values of ω_{p1} , ω_{p2} , and ℓ_{12} , instability occurs in general ($|\ell_{12}| \neq 1$) for ω_{g12} larger than a critical value but smaller than a second larger critical value. The maximum growth rate is for $(\omega_{p2} - \omega_{p1})/\omega_{g12} = -1 - |\ell_{12}|$ (so that $\omega_{p2} < \omega_{p1}$), and it is $\max(\omega_i) = \omega_{g12} |\ell_{12}|^{\frac{1}{2}}$. This is a *dynamical instability* in that it does not depend on dissipation as in the case of a single ring with $\Delta^2 < 0$. For conditions of maximum growth, $\Theta_1/\Theta_2 = -i/|\ell_{12}|^{\frac{1}{2}}$, so that $\theta_1/\theta_2 = |L_2/L_1|^{\frac{1}{2}}$ and $\varphi_1 - \varphi_2 = \pi/2$. We can thus view the co-rotating ring as ‘torquing up’ the more slowly precessing counter-rotating ring by the gravitational interaction or vice-versa.

Figure 11a shows the ω_{g12} dependence of the frequencies of the two slow-precession modes obtained from equation (43) for the case where ring 2 is counter-rotating ($\Omega_2 < 0$) and ring 1 is co-rotating ($\Omega_1 > 0$) and the halo is *oblate*. Figure 11b shows that the mode ω_1 with prograde precession involves mainly motion of ring 2, whereas the ω_2 mode with retrograde precession involves mainly ring 1. For the conditions studied ($\omega_{g12} \leq 0.1\Omega_1$), we find no phase-locking.

2.5. Three Tilted Rings

Extension of the results of Subsection 2.2 to the case of three tilted rings is straightforward. Figure 12a shows the dependence of the three slow precession frequencies on the strength of the gravitational interaction measured by ω_{g12} with $\omega_{g23}/\omega_{g12} = \text{Const}$. For increasing ω_{g12} , the slowest mode (ω_1) *slowly* approaches the limiting frequency given by the generalization of equation (47) to three rings. The other two frequencies decrease monotonically with increasing ω_{g12} . Figure 12b shows the geometrical nature of the three slow precession modes. Figure 13 shows sample orbits $\Theta_j(t)$ for three rings for cases of weak and strong coupling. Figure 14 shows different cases of phase-locking for a three ring system.

3. N Tilted Corotating Rings

The generalization of equation (40) gives the Lagrangian for an N ring system as

$$\begin{aligned} \mathcal{L} = & \frac{1}{2} \sum_{j=1}^N I_j \left(\dot{\theta}_j^2 + \theta_j^2 \dot{\varphi}_j^2 - 2\Omega_j \theta_j^2 \dot{\varphi}_j - \Delta_j^2 \theta_j^2 \right) \\ & - \frac{1}{2} \sum_{j < k} C_{jk} \left[\theta_j^2 + \theta_k^2 - 2\theta_j \theta_k \cos(\varphi_j - \varphi_k) \right]. \end{aligned} \quad (53a)$$

The Hamiltonian,

$$\mathcal{H}(\theta_j, \varphi_j, P_{\theta_j}, P_{\varphi_j}) = \sum_k \left(\dot{\theta}_k \frac{\partial \mathcal{L}}{\partial \dot{\theta}_k} + \dot{\varphi}_k \frac{\partial \mathcal{L}}{\partial \dot{\varphi}_k} \right) - \mathcal{L}$$

is

$$\begin{aligned} \mathcal{H} = & \sum_{j=1}^N \left[\frac{P_{\theta_j}^2}{2I_j} + \frac{1}{2I_j} \left(\frac{P_{\varphi_j}}{\theta_j} + \Omega_j \theta_j \right)^2 + \frac{I_j}{2} \Delta_j^2 \theta_j^2 \right] \\ & + \frac{1}{2} \sum_{j < k} C_{jk} \left[\theta_j^2 + \theta_k^2 - 2\theta_j \theta_k \cos(\varphi_j - \varphi_k) \right]. \end{aligned} \quad (53b)$$

Because the $\{C_{ij}\}$ are non-negative, all of the terms in \mathcal{H} are non-negative if $\Delta_j^2 \geq 0$ which is the case for oblate halo. Thus the N -ring system with $\Delta_j^2 > 0$ is stable in the presence of dissipative forces. The total canonical angular momentum is

$$P_{\varphi}^{tot} = \sum_{j=1}^N \frac{\partial \mathcal{L}}{\partial \dot{\varphi}_j} = \sum_{j=1}^N I_j \theta_j^2 (\dot{\varphi}_j - \Omega_j). \quad (53c)$$

In the absence of dissipation $\mathcal{E}_{rings} = \mathcal{H}$ and $\mathcal{P}_{rings} = -P_{\varphi}^{tot}$ are constants of the motion.

As in the case of one or two rings, it is useful to let

$$\Theta_j(t) = \theta_{jx}(t) - i\theta_{jy}(t) = \theta_j(t) \exp[-i\varphi_j(t)]. \quad (54)$$

The equations of motion can then be written as

$$\begin{aligned} I_j \left(\frac{d^2}{dt^2} + 2i\Omega_j \frac{d}{dt} \right) \Theta_j = \\ -\Delta_j^2 I_j \Theta_j - \sum_{k \neq j} C_{jk} (\Theta_j - \Theta_k), \end{aligned} \quad (55)$$

with $j = 1..N$, where the C_{jk} generalize C_{12} of equation (34).

As discussed in §2.1, a Newtonian drag force on the ring motion due to dynamical friction with the halo matter can be taken into account by including the term

$$-\beta_j I_j \frac{d\Theta_j}{dt} \quad (56)$$

on the right hand side of equation (55). The influence of the relative friction discussed in §2.3 can be accounted for by including the terms

$$-\beta'_{j+\frac{1}{2}} I_{j+\frac{1}{2}} (\dot{\Theta}_j - \dot{\Theta}_{j+1}) - \beta'_{j-\frac{1}{2}} I_{j-\frac{1}{2}} (\dot{\Theta}_j - \dot{\Theta}_{j-1}) \quad (57)$$

on the right hand side of equation (55). Here, $I_{j \pm \frac{1}{2}} \equiv (I_j I_{j \pm 1})^{\frac{1}{2}}$ and $\beta'_{j \pm \frac{1}{2}} \equiv \beta_j \beta_{j \pm 1} = [\nu_t / (\Delta r)^2]_{j \pm \frac{1}{2}}$ with $\beta'_{\frac{1}{2}} = 0$ and $\beta'_{N+\frac{1}{2}} = 0$. With the dissipation terms (56) and (57) included one can readily show that $d\mathcal{E}_{rings}/dt \leq 0$ (see also §4). We have not found an analogous result for $d\mathcal{P}_{rings}/dt$ in the presence of dissipation.

We have developed and tested codes to solve equations (55) (including the terms (56) and (57)) for $N = 7, 13, 25$, and 49 rings. For the results presented here, the rings are taken to be uniformly spaced in r with ring one at $r_1 = 10$ kpc and ring N at $r_N = 40$ kpc so that $r_j = 10 + (j-1)\Delta r$,

with $\Delta r = 30/(N - 1)$ in units of kpc. The ring masses $M_j = 2\pi r_j \Delta r \Sigma(r_j)$ and moments of inertia $I_j = M_j r_j^2$ are calculated with $\Sigma(r_j)$ the sum of the surface density of the inner exponential disk and that of the neutral hydrogen given in §2. The Δ_j^2 are calculated using equations (4), (6), and (18). The coupling coefficients $\{C_{jk}\}$ are evaluated using equations (34) and (30b) and stored. Equations (55) are solved as four first order equations for θ_{xj} , $\dot{\theta}_{xj}$, θ_{yj} , and $\dot{\theta}_{yj}$. At the same time, an additional equation,

$$\frac{d\varphi_j}{dt} = \frac{\theta_{xj}\dot{\theta}_{yj} - \theta_{yj}\dot{\theta}_{xj}}{\theta_{xj}^2 + \theta_{yj}^2}, \quad (58)$$

is also solved to give $\varphi_j(t)$, which is the line-of-nodes angle relative to the x -axis.

Comparisons of the temporal responses of 25 and 49 ring systems for different initial conditions show generally good agreement of the warps Θ_j for the time intervals studied. This indicates that $N = 49$ rings gives a valid representation of a continuous disk. However, in contrast with a continuous disk (HT), an N -ring disk has $2N$ discrete modes with separate frequencies - N ‘low-frequency’ modes and N ‘high-frequency’ modes. Figure 15 shows the power spectrum of $\theta_{x25}(t)$ for a 49 ring disk-halo system which is initially given a random perturbation with all radial wavelengths excited and no damping. The frequencies ω are normalized by the angular velocity of the inner ring Ω_1 . Note that $P_1 \equiv 2\pi/\Omega_1 \approx 0.308$ Gyr for our reference values. The frequency differences between adjacent modes is $\delta\omega \sim \Omega_1/N$. For treatment of initial value problems of disk warping for time intervals $\leq t_{max}$, frequency differences $\delta\omega$ less than $1/t_{max}$ are irrelevant. It is sufficient to have $\delta\omega \sim 1/t_{max}$ which corresponds to $N \sim \Omega_1 t_{max} = 2\pi(t_{max}/0.3\text{Gyr})$ rings. This suggests that a larger number of rings may be needed for our cases with $t_{max} \geq 8$ Gyr (Figures 18 and 19). This will be investigated in a future work.

The lowest frequency mode of the power spectrum, ω_1 in Figure 15 (see also §2.3 and §2.5), remains discrete (that is, isolated) as $N \rightarrow \infty$ because our disk model has a sharp outer edge so that $1/\Sigma(r)$ is integrable (HT; Sparke and Casertano 1988). Power spectra obtained for cases with $C_{jk} \rightarrow \gamma C_{jk}$ show that ω_1 increases with γ much more slowly than the higher frequency modes which is consistent with the behavior observed in Figures 6 and 12. For the conditions of Figure 15, the magnitude ω_1 is considerably smaller than that predicted for the limit of strong self-gravity

between the rings where $\omega_1 \rightarrow \sum L_j \omega_{pj} / \sum L_j$ [equation(47)]. This limiting frequency is the same as the frequency ω_t of Sparke and Casertano (1988). In any case, the frequency ω_1 is so small (the corresponding period is > 8 Gyr) that it is irrelevant to the initial value problems considered below.

In the following four subsections we consider different possible origins of warps in an otherwise flat galaxy. Subsection 3.1 discusses warp excitation by a passing compact satellite; §3.2 treats warp excitation by a compact sinking satellite; §3.3 treats the case of a tilted halo potential. Subsection 3.4 considers the tilt evolution for the case where the initial plane of the disk material is tilted.

3.1. Warp Excitation by a Passing Satellite

Consider the excitation of a warp in a galaxy due to the passage of a satellite of mass M_s much less than the galaxy’s mass. The satellite’s orbit $\mathbf{r}_s(t)$ can easily be calculated exactly for $M_s \rightarrow 0$, neglecting the back reaction of the perturbed galaxy on the satellite. However, we assume that even at closest approach the satellite is far from the center of the galaxy and therefore calculate the orbit in the halo potential, equation (6a), with the ellipticity of the halo neglected for simplicity ($q = 1$). At the closest approach at $\min(|\mathbf{r}_s|) \equiv r_{so}$, the satellite’s speed is v_{so} , and the angle between the satellite and the (x, y) plane is θ_{so} . Also, at closest approach, the satellite is taken to be at $(\mathbf{r}_s)_y = 0$ and $(\mathbf{r}_s)_z > 0$. We consider both prograde and retrograde satellite passages.

In the presence of a satellite of finite mass M_s , the description of the galaxy disk in terms of tilted circular rings breaks down. The centers of the rings are shifted from the origin, and the rings become non-circular. For this reason we consider the response of the galaxy to a ‘symmetrized’ perturbation of a satellite obtained by replacing the actual satellite by two satellites, each of equal mass $M_s/2$, with one satellite in the orbit $\mathbf{r}_s(t)$ described above and the other in the orbit $-\mathbf{r}_s(t)$. With this prescription we then calculate the torque of the satellites on each ring as a function of time,

$$\mathbf{T}_j^s(t) = \frac{1}{2} M_j \int_0^{2\pi} \frac{d\phi}{2\pi} \mathbf{r}_j \times \left[- \frac{\partial}{\partial \mathbf{r}_j} \Phi_s(\mathbf{r}_j, \mathbf{r}_s) \right] + (\mathbf{r}_s \rightarrow -\mathbf{r}_s), \quad (59)$$

where $\mathbf{r}_j(t) = [r_j \cos\phi, r_j \sin\phi, h_j(\phi, t)]$, with $h_j(\phi, t)$ given by equation (8a), is the position vector to a

point on the j th ring, and $j = 1, \dots, N$ runs over the different rings. Here, $\Phi_s = -GM_s/[(\mathbf{r}_j - \mathbf{r}_s)^2 + a^2]^{\frac{1}{2}}$ is the gravitational potential of the satellite and a is its characteristic radius. To obtain the warp response of the galaxy we evaluate equations (59) numerically for $j = 1, \dots, N$ and include the complex torques $\mathcal{T}_j^s(t) = T_{jx}^s(t) - iT_{jy}^s(t)$ on the right hand sides of equations (55).

Figure 16a shows the Briggs plot of the warp response $\theta(\varphi)$ of the galaxy resulting from the retrograde passage of a satellite of mass $M_s = 2 \times 10^{10} M_\odot$. Note that the dependence of $\theta(\varphi)$ at the times shown is of the form of a *leading* spiral wave and that it is qualitatively similar to the leading spiral waves observed in many warped galaxies (Briggs 1990). Note also that the form of the spiral wave is preserved for a long time. However, the amplitude of the warp θ is significantly smaller than the warps observed in many cases, and this agrees with the conclusions of HT. Nevertheless, it is of interest to understand the behavior. Figure 16b shows the warp response for the retrograde case with and without gravitational interactions (C_{jk}) between the rings. Clearly these interactions give a strong phase-locking of the inner rings of the disk (roughly, r_1 to r_{14} or 10 to 18 kpc) which have the same φ_j 's as a function of time. The phase-locking of two and three rings was discussed in §2.2 and §2.4.

Figure 17a shows the Briggs plot for the warp resulting from the prograde passage of the satellite. For early times ($t \leq 2$ Gyr) the form of $\theta(\varphi)$ is a *trailing* spiral wave which is distinctly different from that for the retrograde passage at a similar time. The amplitude of the warp is noticeably larger than for the retrograde case but still smaller than many observed warps. For later times ($t \geq 4$ Gyr) the trailing wave ‘unwraps,’ evolving into a leading spiral wave of form similar to that for the retrograde passage for radial distances out to about 35 kpc. For larger r , the $\theta(\varphi)$ curve has a ‘spur’ where θ increase with r while φ remains roughly constant (see §3.2). This unwrapping appears to be due to the phase-mixing of the fast precession modes which propagate over the radial extent of the disk in times less than 4 Gyr.

The different behavior of the prograde and retrograde cases for early times ($t \leq 1$ Gyr) can be understood by considering the response of a single ring with or without gravitational interactions between rings. Figure 17b shows the orbits [$\theta_{jx}(t)$, $\theta_{jy}(t)$] of ring No. 25 (radius $r_{25} = 25$ kpc) including the gravitational

interactions for prograde and retrograde encounters. Consider the torque on the j^{th} ring $\mathcal{T}_j^s = T_{jx}^s - iT_{jy}^s$ which enters on the right hand side of equation (55). The tilting of the ring during the encounter is relatively small and can be neglected for this discussion. Consequently, $T_{jy}^s(t)$ is an even function of t if the pericenter is taken as $t = 0$. Further, $T_{jy}^s(t)$ is the same for prograde and retrograde encounters. For the considered geometry of the satellite orbit, $T_{jy}^s(0) < 0$, and the magnitude of $T_{jy}^s(t)$ decreases monotonically with increasing $|t|$. On the other hand, the x -torque $T_{jx}^s(t)$, although smaller in magnitude, is an odd function of time, and it has opposite signs for prograde and retrograde encounters. Very roughly $T_{jx}^s(t) \propto d[T_{jy}^s(t)]/dt$ for the prograde case whereas $T_{jx}^s(t) \propto -d[T_{jy}^s(t)]/dt$ for the retrograde case. As a function of time, \mathcal{T}_j^s traces out a closed *clockwise* path in the complex plane for the prograde case, whereas this path is *counterclockwise* for the retrograde case. For the prograde case, the path of \mathcal{T}_j^s is in the same clockwise sense as the path of the orbit $\Theta_j = \theta_{xj} - i\theta_{yj}$ for the *fast* precession mode (see §2.1), whereas for the retrograde case the path of \mathcal{T}_j^s is in the same direction of motion as Θ_j for the *slow* precession mode. For this reason a prograde encounter couples strongly to the fast precession mode, whereas a retrograde encounter couples mainly to the slow precession mode.

3.2. Warp Excitation by a Sinking Satellite

Here, we discuss the behavior of warps excited by a slowly sinking compact minor satellite. The satellite is assumed to be minor in the respect that its mass is much smaller than that of the galaxy plus halo matter within say 30 kpc. The sinking of a more massive satellite is likely to cause substantial thickening of the disk (Walker, Mihos, and Hernquist 1996) which is not observed. Initially, the satellite is assumed to be in an approximately circular bound orbit in the halo gravitational potential at a large radius r_{so} in the (x, z) plane at an angle θ_{so} above the (x, y) plane. The satellite slowly sinks owing to dynamical friction with the halo matter [equation (6a) with $q = 1$] which in the simplest description (BT, p. 428) causes the specific angular momentum of the satellite $\ell_s \approx r_s(t)v_o$ to decrease as

$$\frac{d\ell_s}{dt} \approx -0.428 \frac{GM_s}{r_s(t)} \ell_n \Lambda, \quad (60a)$$

where $\ell n\Lambda$ is the Coulomb logarithm. The time for the satellite to sink from r_{so} to the galaxy's center is

$$t_{sink} \approx 4.40 \text{ Gyr} \left(\frac{10^{10} M_\odot}{M_s} \right) \left(\frac{r_{so}}{50 \text{ kpc}} \right)^2 \times \left(\frac{v_o}{200 \text{ km/s}} \right) \left(\frac{3}{\ell n\Lambda} \right). \quad (60b)$$

The disk response is found by integrating equations (55) including the numerically evaluated torques (59) for $\mathbf{r}_s(t)$ at each time step for a 'symmetrized' sinking analogous to the approach discussed in §3.1.

Figure 18 shows the Briggs plots of the warp response $\theta(\varphi)$ of the galaxy at different times after the sinking ($\mathbf{r}_s = 0$) of a satellite of mass $M_s = 10^{10} M_\odot$ in retrograde and prograde orbits. A number of points are observed:

(1) The warp amplitudes are larger than for the passing satellite (of mass $M_s = 2 \times 10^{10} M_\odot$) discussed in §3.1, but the amplitudes are still smaller than some observed warps (Briggs 1990).

(2) Coiling in the $\theta(\varphi)$ curves at early times ($t \leq 2$ Gyr) tends to disappear at later times ($t \geq 4$ Gyr). We believe but have not proven that this is due to the phase-mixing of the fast precession modes which propagate over the radial extent of the disk in times < 4 Gyr (see also §3.1).

(3) For both the retrograde and prograde cases $\theta(\varphi)$ exhibits a leading spiral wave for $t \geq 4$ Gyr qualitatively of the form observed for M 83 (see Figure 2c). However, the tilt amplitude θ is significantly smaller than that for M 83.

The dissipative torques due to dynamical friction [equation (56)] and that due to relative friction [equation (57)] have different consequences for the warp evolution. For a dynamical friction coefficient $\beta_j/\Omega_1 = 0.1$, the warp amplitudes θ for the cases of Figures 18a and 18b are reduced by factors ~ 0.5 while the line-of-nodes angles are roughly the same. On the other hand, for relative friction coefficients $\beta'_j/\Omega_1 \leq 1$, short radial wavelengths are damped out without appreciably affecting the overall shape of the $\theta(\varphi)$ curves.

3.3. Tilted Halo Potential

Dekel and Shlosman (1983) and Toomre (1983) proposed that observed warps of galaxies may result from the fact that the dark matter halo is oblate and is rigidly tilted with respect to the inner disk. To

consider this possibility we generalize equation (55) to the case of N tilted rings in a halo potential which is rigidly tilted by an angle, say, $\Theta_h = \theta_{hx}$ (with $\theta_{hx}^2 \ll 1$) with respect to the z -axis of the inner disk. We find

$$I_j \left(\frac{d^2}{dt^2} + 2i\Omega_j \frac{d}{dt} \right) \Theta_j = -\Delta_{dj}^2 I_j \Theta_j - \Delta_{hj}^2 I_j (\Theta_j - \Theta_h) - \sum_{k \neq j}^N C_{jk} (\Theta_j - \Theta_k), \quad (61)$$

where $\Delta_{dj}^2 \equiv \kappa_{idzj}^2 - \Omega_{idj}^2$ and $\Delta_{hj}^2 \equiv \kappa_{hzzj}^2 - \Omega_{hj}^2$. The damping terms are still given by equations (56) and (57).

For a special disk tilt, $\Theta_j^L = \text{funct.}(j)$, the right-hand-side of equation (61) is zero so that Θ_j^L is time-independent. This Θ_j^L corresponds to the Laplacian surface of the disk (BT, p. 413). It is given by

$$\sum_{k=1}^N \mathcal{M}_{jk} \Theta_k^L = \Delta_{hj}^2 \Theta_h,$$

$$\mathcal{M}_{jk} = \left(\Delta_{dj}^2 + \Delta_{hj}^2 + \frac{1}{I_j} \sum_{\ell} C_{j\ell} \right) \delta_{jk} - \frac{1}{I_j} C_{jk} (1 - \delta_{jk}), \quad (62)$$

where δ_{jk} is the Kronecker delta and the prime on the summation means that the diagonal terms are omitted. The damping terms (56) and (57) are of course zero for the Laplacian tilt. If the self-gravity of the rings (C_{jk}) is negligible, $\Theta_j^L = [\Delta_{hj}^2 / (\Delta_{hj}^2 + \Delta_{dj}^2)] \Theta_h$. Equation (62) can always be inverted to give Θ_j^L if $\Delta_j^2 > 0$. This is because the N -ring system is stable for $\Delta_j^2 > 0$ (see discussion following equation (53b)) which implies $\det(\mathcal{M}_{jk}) > 0$.

A general solution of equation (61) can evidently be written as $\Theta_j(t) = \Theta_j^L + \Theta'_j(t)$, where Θ'_j obeys equation (55) which has no reference to the halo tilt. Over a sufficiently long period of time, damping given by equation (56) and/or (57) will give $\Theta'_j(t) \rightarrow 0$ as discussed in the paragraph after next.

Figure 19a shows the Laplacian tilt Θ_j^L for a representative case with and without the self-gravity of the rings. Figure 19b shows the Briggs plots $\theta(\varphi)$ at times $t = 4$ and 8 Gyr for a disk started from a Laplacian tilt and from a 20% deviation from a Laplacian tilt. The Briggs plot for the Laplacian tilt is in contrast with the leading spiral wave observed, for example, in M 83 (Figures 1 and 2) (Briggs 1990). However, the

Laplacian tilt may be relevant to cases such as NGC 3718 which shows a relatively straight line-of-nodes.

There is no evident reason for a disk to be initially ‘set up’ in a Laplacian tilt. Figure 19b shows that deviations from the Laplacian tilt evolve to give a line-of-nodes which is not straight. As mentioned, dissipative torques due to dynamical friction [equation (56)] and/or relative friction [equation(57)] act to damp out the deviation (Θ'_j) from the Laplacian tilt over a period of time. For example, for $\beta_j/\Omega_1 = 0.1$ in equation (56) and no relative friction, the maximum line-of-nodes deviation (φ_{49}) at 8 Gyr is reduced by a factor ~ 0.4 from the case with no dissipation shown in Figure 19b. On the other hand for $\beta'_j/\Omega_1 = 1.0$ and no dynamical friction, the maximum line-of-nodes deviation is reduced by a factor ~ 0.5 .

3.4. Initially Tilted Disk Plane

Here we consider the possibility that at some initial time an outer gaseous disk is formed which is tilted with respect to the plane of the inner disk. This situation could arise by the capture, tidal-disruption, radial-spreading, and cooling of a low mass gas cloud by a disk galaxy. For a spherical cloud of mass M_{cl} and radius a_{cl} in an approximately circular orbit of radius r , tidal breakup occurs roughly for $a_{cl} \gtrsim \frac{2}{5}(GM_{cl}r^2/v_o^2)^{\frac{1}{3}} \approx 3\text{kpc}(M_{cl}/10^{10}M_\odot)^{\frac{1}{3}}(r/20\text{kpc})^{\frac{2}{3}}(200\text{km/s}/v_o)^{\frac{2}{3}}$, where v_o is the circular velocity in the flat rotation region of the galaxy [equation (6b)]. Treatment of the cloud disruption is beyond the scope of the present work. Instead, we study the initial value problem where at $t = 0$ there is a smooth transition from an untilted inner disk to a tilted outer disk with a straight line-of-nodes. Specifically, we take

$$\Theta_j(t=0) = \frac{\theta_{xo}}{2} \left\{ 1 - \cos[\pi(r_j - r_1)/(r_N - r_1)] \right\}, \quad (63a)$$

$$\frac{d\Theta_j(t=0)}{dt} = 0, \quad (63b)$$

where θ_{xo} is the initial tilt angle of the outer disk. Similar behavior is found for other smooth variations of Θ_j . The smooth variation of Θ_j avoids the excitation of short radial wavelength modes.

Figure 20 shows the nature of the warp evolution resulting from the initial conditions (63). Figure 21 shows a surface plot of the disk at $t = 2$ Gyr. A leading spiral wave appears in the Briggs plot (panel c), and its amplitude grows with time. Progressively, the interior region of the disk (say, $10 \leq r \leq 25$ kpc)

flattens to the plane of the inner disk while the exterior region warp amplitude θ grows. The dependences shown in Figure 20 for $t = 2 - 4$ Gyr are *qualitatively* similar to those observed for M 83 (see Figure 2). The outer part of the disk shows an inverse power law dependence of the line-of-nodes φ on r (panel b of Figure 20) which is qualitatively similar to that for M 83 where $\varphi \propto r^{-1.5}$.

The dissipative torques due to dynamical friction [equation (56)] and that due to relative friction [equation (57)] affect the results of Figure 20 in different ways. For a dynamical friction coefficient $\beta_j/\Omega_1 = 0.1$, and no relative friction, the maximum warp amplitude at $t = 4$ Gyr is reduced by about 30%. On the other hand, for no dynamical friction, but a relative friction coefficient $\beta'_j = 1.0$, the warp at $t = 4$ Gyr is essentially unchanged.

4. Continuum Limit

In the continuum limit, the Hunter and Toomre (1969) equation for the vertical displacement of the disk $h(r, \phi, t)$ can be obtained from equation (55) by recalling that $h = r\theta_x(t)\sin\phi - r\theta_y(t)\cos\phi = \mathcal{I}m[r\Theta \exp(i\phi)]$. We omit for the moment the damping terms (56) and (57). Multiplying equation (55) by $r \exp(i\phi)$ and taking the imaginary part gives

$$I_j \left(\frac{\partial}{\partial t} + \Omega_j \frac{\partial}{\partial \phi} \right)^2 h_j = -I_j (\Omega_j^2 + \Delta_j^2) h_j - \sum_{k \neq j}^N C_{jk} h_k + \sum_{k \neq j}^N C_{jk} r_j h(r_k, \phi, t)/r_k, \quad (64)$$

where the left hand side of this equation follows from the same steps as for equation (21), where $h_j = h(r_j, \phi, t)$, and where $I_j = 2\pi r_j^3 \Delta r \Sigma(r_j)$ with Δr taken as a constant for simplicity. The continuum limit is $N \rightarrow \infty$ and $\Delta r \propto 1/N \rightarrow 0$.

From the definitions (14) and (18), we have on the right hand side of equation (64), $\Omega_j^2 + \Delta_j^2 = \bar{\kappa}_{jz}^2 + \Omega_j^2 - \bar{\Omega}_j^2$. From the decomposition of the potential (§1), it is clear that $\Omega_j^2 - \bar{\Omega}_j^2$ is the contribution to the disk rotation from the outer disk; that is,

$$\Omega_j^2 - \bar{\Omega}_j^2 = \frac{1}{r} \frac{\partial \Phi_{od}}{\partial r} = \frac{G}{r} \int d^2 r' \frac{\Sigma(r') [r - r' \cos(\phi')]}{[r^2 + (r')^2 - 2rr' \cos(\phi')]^{\frac{3}{2}}}, \quad (65)$$

where $d^2r' = r' dr' d\phi'$, and where the integration is over the outer part of the disk, $r \geq r_1$, with r_1 chosen to be significantly larger than the scale-length r_d of the inner disk (see §2). Note that the summations in equation (64) are also over the outer part of the disk. Thus, one term which contributes to the right hand side of equation (64) is

$$-I_j(\Omega^2 - \bar{\Omega}_j^2)h_j = -GI_j h_j \int d^2r' \frac{\Sigma' [r - r' \cos(\phi')]}{r [\dots]^{\frac{3}{2}}}, \quad (66a)$$

where $\Sigma' \equiv \Sigma(r')$, and the factor in the denominator to the 3/2 power is the same as in equation (65). Using the definition of C_{jk} in equation (34), the first sum on the right hand side of equation (64) can be converted to an integral in the continuum limit,

$$\sum_1 = -GI_j h_j \int d^2r' \frac{\Sigma' r' \cos(\phi')}{r [\dots]^{\frac{3}{2}}}. \quad (66b)$$

Similarly, the continuum limit of the second sum in equation (64) gives

$$\begin{aligned} \sum_2 &= GI_j \int d^2r' \frac{\Sigma' h(r', \phi, t) \cos(\phi - \phi')}{[r^2 + (r')^2 - 2rr' \cos(\phi - \phi')]^{\frac{3}{2}}}, \\ &= GI_j \int d^2r' \frac{\Sigma' h(r', \phi', t)}{[r^2 + (r')^2 - 2rr' \cos(\phi - \phi')]^{\frac{3}{2}}}, \end{aligned} \quad (66c)$$

in view of equation (31c).

Combining equations (64)-(66) and dropping the j subscripts gives

$$\begin{aligned} \Sigma \left(\frac{\partial}{\partial t} + \Omega \frac{\partial}{\partial \phi} \right)^2 h &= -\Sigma \bar{\kappa}_z^2 h \\ -G\Sigma \int d^2r' \frac{\Sigma' (h - h')}{[r^2 + (r')^2 - 2rr' \cos(\phi - \phi')]^{\frac{3}{2}}}, \end{aligned} \quad (67)$$

where $h' \equiv h(r', \phi', t)$. Note that $\bar{\kappa}_z$ includes the vertical restoring force of the inner disk and the halo. Thus, equation (67) is the same as Hunter and Toomre's (1969) equation for h , in that they did not separate out the inner disk and did not include a halo potential.

The Newtonian drag term (56) due to dynamical friction gives a contribution

$$-\beta \Sigma \frac{\partial h}{\partial t} \quad (68)$$

on the right hand side of equation (67). The damping term (57) due to relative friction between the rings

gives a contribution

$$\frac{1}{r^2} \frac{\partial}{\partial r} \left[\nu_t \Sigma r^3 \frac{\partial}{\partial r} \left(\frac{1}{r} \frac{\partial h}{\partial t} \right) \right] \quad (69)$$

on the right hand side of equation (67).

Multiplying equation (67) by $2d^2r(\partial h/\partial t)$, integrating over the outer disk, and following the steps of HT (their Appendix B) gives, in the absence of dissipation, the constant of the motion

$$\begin{aligned} \mathcal{E}_{warp} &= \int d^2r \Sigma \left[\left(\frac{\partial h}{\partial t} \right)^2 + \Delta^2 h^2 \right] \\ &+ \frac{G}{2} \int_0^\infty dr r^2 \Sigma \int_0^\infty dr' (r')^2 \Sigma' \int_0^{2\pi} d\phi \times \\ &J(r, r') \left[\frac{h(r', \phi, t)}{r'} - \frac{h(r, \phi, t)}{r} \right]^2, \end{aligned} \quad (70)$$

where $J(r, r')$ is given by equation (30b). Substituting $h(r, \phi, t) = r\theta(t)\sin[\phi - \varphi(t)]$ from equation (8a), one readily finds that \mathcal{E}_{warp} is identical to $\mathcal{E}_{rings} = \mathcal{H}$ of equation (53b). Note that \mathcal{E}_{warp} is non-negative and therefore the disk is stable if $\Delta^2(r) \geq 0$.

Including the dissipation terms (68) and (69) gives

$$\begin{aligned} \frac{d\mathcal{E}_{warp}}{dt} &= -2 \int d^2r \beta \Sigma \left(\frac{\partial h}{\partial t} \right)^2 \\ &- 2 \int d^2r \nu_t \Sigma \left[r \frac{\partial}{\partial r} \left(\frac{1}{r} \frac{\partial h}{\partial t} \right) \right]^2. \end{aligned} \quad (71)$$

The relative friction is of course zero if h/r is a function only of time which corresponds to a rigid tilt.

The second constant of the motion \mathcal{P}_{rings} , found in §2.1 and §3 [equation (53c)], can of course be expressed in terms of $h(r, \phi, t)$ in the continuum limit. Instead, we obtain this new constant directly from the HT equation for h by multiplying equation (67) by $2d^2r(\partial h/\partial \phi)$ and integrating over the outer disk. This gives

$$\begin{aligned} \mathcal{P}_{warp} &= 2 \int d^2r \Sigma \left[\Omega \left(\frac{\partial h}{\partial \phi} \right)^2 + \frac{\partial h}{\partial \phi} \frac{\partial h}{\partial t} \right] = \text{Const.} \\ &= \int d^2r \Sigma r^2 \theta^2 (\Omega - \dot{\varphi}), \end{aligned} \quad (72)$$

and $\mathcal{P}_{warp} = \mathcal{P}_{rings}$ in the continuum limit, in the absence of dissipation. With dissipation included, we have not found a simple expression for $d\mathcal{P}_{warp}/dt$.

5. Conclusions

This paper develops a representation for the anti-symmetric small amplitude warp dynamics of a self-gravitating disk in terms of N tilted concentric rings. That is, we consider only azimuthal mode number of the warp $m = 1$ (or -1). This representation is suggested by the kinematic ring model of Rogstad et al. (1974) which is used in interpreting HI disk warps (Briggs 1990). The rings are considered to be in a fixed oblate (or prolate) halo potential and in the potential of an inner, untilted disk. Different initial value problems are studied using our N -ring model.

We first consider in detail the tilting dynamics of one ring in the potential of the halo and inner disk. The equations of motion are shown to have a particularly simple form when written in terms of the complex tilt angle $\Theta = \theta \exp(-i\varphi)$, where θ is the actual tilt angle, and φ is the angle of the line-of-nodes relative to the inertial x -axis. The single ring has a slow and a fast precession mode which are analogous to the normal modes of vibration of a non-rotating mechanical system. For the slow (fast) mode $\Theta(t)$ rotates in the clockwise (counter clockwise) direction in the complex plane. The dynamical equation for Θ of course has an energy constant of the motion, \mathcal{E}_{ring} . Additionally, we show that there is a second constant of the motion. By writing out the Lagrangian for one ring, $\mathcal{L} = \mathcal{L}(\theta, \dot{\theta}, \varphi, \dot{\varphi})$, this constant of the motion is recognized as the canonical angular momentum for the φ coordinate, $P_\varphi = \partial\mathcal{L}/\partial\dot{\varphi} = \text{Const}$.

We examine the influence of the drag on the motion of one ring through the halo matter due to dynamical friction. The full calculation of this drag (Nelson and Tremaine 1995) is beyond the scope of this work. Instead, we include a linear drag torque in the equation of motion for Θ which we estimate following the approach of Weinberg (1985). Inclusion of this term shows that dissipation can destabilize the ring tilting in a prolate halo potential. The instability is of the negative energy type; that is, it occurs only for $\mathcal{E}_{ring} < 0$.

We next consider the particularly interesting case of two tilted, gravitationally interacting rings of different radii in the potential of the halo and inner disk. We derive dynamical equations for $\Theta_1 = \theta_1 \exp(-i\varphi_1)$ and $\Theta_2 = \theta_2 \exp(-i\varphi_2)$. This case shows the phenomenon of phase-locking of the line-of-nodes of the two rings. The gravitational interaction between the two rings is appropriately measured by the coupling

strength ξ_{12} of equation (48). As ξ_{12} increases the ring motion changes from that of independent precession for $\xi_{12} < 1$ to phase-locked precession for $\xi_{12} > 1$ where the lines-of-nodes coincide approximately, $\varphi_1 \approx \varphi_2$. This phase-locking persists for the case of $N > 2$ rings.

We examine the influence of dissipative forces on the tilting motion of two rings. In addition to dynamical friction, which is included as linear drag torques on each ring, we include the ‘relative’ friction which can result from the differential vertical motions of two gaseous rings due to turbulent viscosity. The corresponding drag torques on each ring have a definite form owing to the requirement that the total angular momentum of the two rings be conserved in the absence of external torques. The turbulent viscosity is assumed to be described by the α model of Shakura (1973) and Shakura and Sunyaev (1973). We find that the relative friction, as well as the dynamical friction, can destabilize the motion of two rings in a prolate halo potential.

We study the case of two tilted rings which rotate in opposite directions. This situation, which is pertinent to observed counter-rotating galaxies (see, for example, Jore, Broeils, and Haynes 1996), is found to be unstable in a prolate halo potential for certain conditions in the absence of dissipation. That is, a dynamical instability may occur.

For the general case of N -tilted, gravitationally interacting rings of radii $r_j = r_1 + (j - 1)\Delta r$ in the potential of the halo and inner disk we obtain equations of motion for $\Theta_j = \theta_j \exp(-i\varphi_j)$ for $j = 1, \dots, N$. The Lagrangian has the form $\mathcal{L} = \mathcal{L}(\theta_j, \dot{\theta}_j, \varphi_j, \dot{\varphi}_j)$, and this gives, in the absence of dissipative torques, both an energy constant of the motion and a total canonical angular momentum constant of the motion, $P_\varphi = \sum_j \partial\mathcal{L}/\partial\dot{\varphi}_j = \text{Const}$. We comment on the numerical solutions for Θ_j for different values of N , and we give a sample power spectrum for $N = 49$ which shows the distribution of the $2N$ mode frequencies. We argue that for treatment of initial value problems of time duration t_{max} , mode frequency differences $\delta\omega$ smaller than $1/t_{max}$ are irrelevant. This leads to the estimate $N = \mathcal{O}(10^2)$ for the number of rings needed to treat warps in galactic disks.

In the continuum limit $N \rightarrow \infty$, the ring model is shown to give the Hunter and Toomre (1969) dynamical equation for the vertical displacement of the disk $h(r, \phi, t)$. Dissipative torques due to dynamical

friction and/or relative friction (for gaseous rings) are shown to cause the energy of the warp \mathcal{E}_{warp} to decrease with time.

We have numerically solved the dynamical equations for Θ_j for $N = 49$ for four different types of initial conditions which may give rise to observed warps in galaxies: (1) warp excitation by a passing satellite with relatively large impact parameter; (2) excitation by a slowly sinking compact minor satellite; (3) warp evolution in a tilted halo potential (Dekel and Shlosman 1983; and Toomre 1983); and (4) warp evolution resulting from an initially tilted disk plane due to the tidal breakup of a gas cloud. The nature of the disk response at different times is most clearly shown in the polar plots of θ_j versus φ_j which we refer to as Briggs plots. This is one of the forms used by Briggs (1990) to describe the warp geometry as deduced by fitting a kinematic ring model (Rogstad et al. 1974) to HI observations.

For case (1) we find that the polar plots $\theta_j(\varphi_j)$ have the shape of a leading spiral wave qualitatively of the form observed, but the warp amplitude θ_j is smaller than observed in many galaxies. The small warp amplitudes found here are in agreement with the conclusions of HT. The leading spiral in the $\theta_j(\varphi_j)$ curves in the outer part of the disk (where the self-gravity between the rings is small) results from the dominance of the slow precession mode which gives very roughly $\dot{\varphi}_j \sim \omega_{pj} \propto -1/r$, where ω_{pj} is the single ring slow precession frequency. The fast precession modes disappear in a few Gyrs due to phase-mixing.

For case (2) of a sinking satellite, we find that the $\theta_j(\varphi_j)$ curves have a large noise component and are unlike the observed curves in the absence of relative friction between the rings. This is due to the violent excitation from the satellite passing through the disk. However, with relative friction included, the $\theta_j(\varphi_j)$ curves are smooth leading spiral waves qualitatively similar in shape to the observed curves. The warp amplitude, although significantly larger than for case (1), is still smaller than that for many observed warps. We find that the inner part of the disk where θ_j is small has an approximately straight line-of-nodes (φ_j independent of j) for both cases (1) and (2) as observed by Briggs (1990) (his ‘rule of behavior’ No. 2). We show that this is due to the above-mentioned phase-locking of the lines-of-nodes of the inner rings of the disk due to self gravity between the rings.

For case (3) of an oblate halo potential rigidly tilted with respect to the inner disk of the galaxy, there is

a unique time independent Laplacian warp $\Theta_j = \Theta_j^L$ (BT, p. 413) which has a straight line-of-nodes ($\varphi_j = \text{Const.}$). However, it is unlikely that a galactic HI disk is ‘set up’ with the Laplacian tilt. Deviations from Θ_j^L evolve to give a line-of-nodes which is not straight. Over the age of the galaxy, the deviations from Θ_j^L may damp out due to dynamical friction and/or relative friction between the rings. This case is possibly relevant to the warp of NGC 3718 which shows an approximately straight line-of-nodes out to $r \approx 1.75R_{Hol}$ (Briggs 1990).

Case (4) of an initially tilted disk plane with a straight line-of-nodes gives: (1) polar plots $\theta_j(\varphi_j)$ for $t \sim 2 - 6$ Gyr with the leading spiral shape qualitatively of the form observed; (2) straight line-of-nodes ($\varphi_j \approx \text{Const.}$) in the inner part of the disk as observed as a result of phase-locking due to self-gravity; and (3) a warp amplitude linearly dependent on the initial tilt of the disk plane. Further, the line-of-nodes angle $\varphi(r)$ in the outer part of the disk is found to have an inverse power law dependence on r qualitatively of the form of shown for M 83 (see Figure 2b).

We thank M.P. Haynes for pointing out the paper of F.H. Briggs (1990) and for valuable discussions which stimulated this work. Further, we thank F.H. Briggs, G. Contopoulos, and M.M. Romanova for valuable discussions. We thank I.L. Tregillis for critical checking of an early version of this work. This work was supported in part by NSF grant AST-9320068.

REFERENCES

- Beal, J.W., Brettschneider, Christofilos, N.C., Hester, R.E., Lamb, W.A., Sherwood, W.A., Spoerlein, R.L., Weiss, P.B., & Wright, R.E. 1969, in *Plasma Physics and Controlled Nuclear Fusion Research* (International Atomic Energy Agency, Vienna), Vol. I, p. 967
- Binney, J. 1992, *Ann. Rev. Astron. Astrophys.*, 30, 51
- Binney, J., & Tremaine, S. 1987, *Galactic Dynamics* (Princeton: Princeton University Press)
- Briggs, F.H. 1990, *ApJ*, 352, 15
- Broeils, A.H., & Rhee, M.H. 1997, *A&A*, in press
- Dekel, A., & Shlosman, I. 1983, in *Internal Kinematics and Dynamics of Galaxies*, E. Athanassoula, Ed. (IAU), p. 187
- Furth, H.P. 1965, *Phys. Fluids*, 8, 2020
- Hunter, C. 1994, in *Waves in Astrophysics*, J.H. Hunter, & R.E. Wilson, Eds., *Ann. New York Acad. Sci.*, V. 773, p. 111
- Hunter, C., & Toomre, A. 1969, *ApJ*, 155, 747
- Jore, K.P., Broeils, A.H., & Haynes, M.P. 1996, *AJ*, 112, 438
- Kahn, F.D., & Woltjer, L. 1959, *ApJ*, 130, 705
- Lynden-Bell, D. 1965 *MNRAS*, 129, 299
- May, A., & James, R.A. 1984, *MNRAS*, 206, 691
- Merritt, D., & Sellwood, J.A. 1994, *ApJ*, 425, 551
- Nelson, R.W., & Tremaine, S. 1995, *MNRAS*, 275, 897
- Rogstad, D.H., Lockhart, I.A., & Wright, M.C.H. 1974, *ApJ*, 193, 309
- Shakura, N.I. 1973, *Sov. Astron.*, 16, 756
- Shakura, N.I., & Sunyaev, R.A. 1973, *A&A*, 24, 337
- Sparke, L.S., & Casterano, S. 1988, *MNRAS*, 234, 873
- Toomre, A. 1983, in *Internal Kinematics and Dynamics of Galaxies*, E. Athanassoula, Ed. (IAU), p. 177
- Walker, I.R., Mihos, J.C., & Hernquist, L. 1996, *ApJ*, 460, 121
- Weinberg, M.D. 1985, *MNRAS*, 213, 451

This 2-column preprint was prepared with the AAS L^AT_EX macros v4.0.

Fig. 1.— Surface plot of the warped disk of M 83 (NGC 5236) obtained from the data of Briggs (1990). The rotation of the galaxy is clockwise so that the warp of the disk is a *leading* spiral wave (Briggs 1990). The scales are in units of 10 kpc for a Holmberg radius of M 83 of $R_{Hol} = 7.3$ arcmin and a distance of M 83 of 5.9 Mpc which assumes a Hubble constant $H_o = 65$ km/s/Mpc (Briggs 1996, private communication). The colors are in 16 steps uniformly spaced between z_{min} and z_{max} .

Fig. 2.— Nature of the warp of the disk of M 83 from Briggs (1990). The top panel (a) shows the radial (r) dependence of the tilt angle $\theta(r)$. The middle panel (b) shows the r -dependence of the angle of the line-of-nodes $\varphi(r)$. The bottom panel (c) shows the dependence of θ on φ , which we refer to as a Briggs plot. The radii are in units of 10 kpc for the parameters mentioned in the caption of Figure 1. In these units the Holmberg radius is $R_{Hol} \approx 1.26$. In panel (b), the dashed curve shows the least-square-fit of a power law dependence to the curve for $1 \leq r \leq 3.4$ which gives $\varphi \approx 216^\circ r^{-1.48}$ (with an R value of 0.993). Note that in the Briggs plot φ has been taken to increase in the clockwise direction to account for the fact that the galaxy rotates in the clockwise direction. Except for our discussion of counter rotating rings, we assume that the matter of the rings (representing the galaxy disk) rotates in the counter-clockwise direction. Note that the data points given here have only an approximate correspondence with those given by Briggs in that we have scanned and digitized the data from his figures.

Fig. 3.— Geometry of one tilted ring of a disk galaxy. For the case shown, the line-of-nodes is along the x -axis, that is, $\varphi = 0$. Also, $\theta_x > 0$, $\theta_y = 0$, and \mathbf{n} denotes the normal to the ring plane.

Fig. 4.— Illustrative single ring orbits for a case shown in (a) where the slow mode is dominant ($C_1 = 0.2$, $C_2 = 0.8$) and in (b) where the fast mode is dominant ($C_1 = 0.8$, $C_2 = 0.2$). For both plots, i corresponds to the starting point, and f to the end point at $t_f = 62.8/\Omega$, and $\Delta^2/\Omega^2 = 0.2$.

Fig. 5.— Dependence of the dimensionless integral J'_{12} defined in equation (45e) on $\delta = r_1/r_2$. The dashed lines correspond to approximations discussed in the text.

Fig. 6.— The top panel (a) shows the dependences of

the two slow precession frequencies of two co-rotating rings in an *oblate* halo on the strength of the gravitational interaction measured by ω_{g12} obtained the full equation (43) and the approximate equation (44). The frequencies are measured in units of Ω_1 . For this figure, $\Omega_1/\Omega_2 = 2$, $I_1/I_2 = 1$, and $\Delta_j^2 = 0.2\Omega_j^2$. [Note that the two fast precession modes, ω_3 and ω_4 , have frequencies 1.05 and 2.1 for $\omega_{g12} = 0$, and 1.19 and 2.19 for $\omega_{g12} = 0.1$. The ω_3 mode has $\Theta_2/\Theta_1 \gg 1$ and thus involves mainly motion of ring 2, whereas the ω_4 mode has $-\Theta_2/\Theta_1 \ll 1$ and involves motion mainly of ring 1.]

– The bottom panel (b) shows the dependences of the amplitude ratios Θ_2/Θ_1 for the two slow precession modes. For small values of ω_{g12} , the ω_1 mode involves motions mainly of ring 2, whereas the ω_2 mode involves motion mainly of ring 1.

Fig. 7.— Illustrative orbits $\{\Theta_1(t), \Theta_2(t)\}$ for two co-rotating rings in an oblate halo for weak (a, top panel) and strong (b, bottom panel) coupling for the same parameters as Figure 6. The initial conditions are $\Theta_1/\Theta_2 = 1/2$ and $\dot{\Theta}_1 = 0 = \dot{\Theta}_2$. The points labeled by f 's all correspond to the final time $t_f = 30\pi/\Omega_1$ (which is arbitrary). The constants of the motion \mathcal{E}_{rings} and \mathcal{P}_{rings} are constant in the numerical integrations with fractional errors $< 10^{-6}$. For the top panel, $\omega_{g12}/\Omega_1 = 0.005$ ($\xi_{12} \approx 0.3$), and the rings precess almost independently. For the bottom panel, $\omega_{g12}/\Omega_1 = 0.015$ ($\xi_{12} \approx 0.9$), and the rings precess together with their lines-of-nodes phase-locked as shown in Figure 8. The dividing value separating independent and phase-locked precession is $\omega_{g12}/\Omega_1 \approx 0.010$ or $\xi_{12} \approx 0.60$. Of course, this value depends on the initial value Θ_1/Θ_2 for $\dot{\Theta}_j(0) = 0$.

Fig. 8.— Azimuthal angle difference of the line-of-nodes of two rings $\varphi_2 - \varphi_1$ for cases (a) and (b) of Figure 7. At the final time $t_f = 30\pi/\Omega_1$, for the phase-locked case $(\varphi_2 - \varphi_1)_f \approx -24^\circ$, whereas for the unlocked case $(\varphi_2 - \varphi_1)_f \approx 253.5^\circ$.

Fig. 9.— The top panel (a) shows the dependences of the two slow precession frequencies of two co-rotating rings in an *prolate* halo on the strength of the gravitational interaction measured by ω_{g12} obtained equation (43). The frequencies are measured in units of Ω_1 . For this figure, $\Omega_1/\Omega_2 = 2$, $I_1/I_2 = 1$, and $\Delta_j^2 = -0.2\Omega_j^2$. – The bottom panel (b) shows the dependences of the amplitude ratios Θ_2/Θ_1 for the two slow precession modes. For small values of ω_{g12} , the ω_1 mode

involves motions mainly of ring 2, whereas the ω_2 mode involves motion mainly of ring 1. For large ω_{g12} the ω_2 mode frequency approaches the limit given in equation (47) and $\Theta_2/\Theta_1 \rightarrow 1$.

Fig. 10.— Region of instability of two rings, one co-rotating ($\Omega_1 > 0$) and the other counter-rotating ($\Omega_2 < 0$), in a prolate halo potential as discussed below equation (51).

Fig. 11.— The top panel (a) shows the dependences of the two slow precession frequencies of two counter rotating rings ($\Omega_1 > 0$ and $\Omega_2 < 0$) in an *oblate* halo on the strength of the gravitational interaction measured by ω_{g12} obtained equation (43). The frequencies are measured in units of Ω_1 . For this figure, $\Omega_1/\Omega_2 = -2$, $I_1/I_2 = 1$, and $\Delta_j^2 = 0.2\Omega_j^2$.

– The bottom panel (b) shows the dependences of the amplitude ratios Θ_2/Θ_1 for the two slow precession modes.

Fig. 12.— The top panel (a) shows the dependence of the three slow precession frequencies of a three ring system on the strength of the gravitational interaction measured by ω_{g12} . The frequencies are measured in units of Ω_1 . For this figure, $(r_1, r_2, r_3) = (1, 2, 3)$, $(\Omega_1, \Omega_2, \Omega_3) = (1, \frac{1}{2}, \frac{1}{3})$, $I_2/I_1 = 1$, $I_3/I_2 = 1$, and $\Delta_j^2 = 0.2\Omega_j^2$. For small values of ω_{g12} , the ω_1 mode involves motion mainly of ring 3, the ω_2 mode motion of ring 2, and the ω_3 mode motion of ring 1. For larger values of ω_{g12} the motions of the different rings become coupled. For large ω_{g12} the slowest mode (ω_1) approaches the limiting value given by the generalization of equation (47) to three rings. [The three fast precession modes have frequencies 0.698, 1.05, and 2.09 for $\omega_{g12} = 0$ and 0.842, 1.30, and 2.20 for $\omega_{g12}/\Omega_1 = 0.1$.]

– The bottom panel (b) shows the r -dependence of the vertical displacements h (along a line \perp to the line-of-nodes) for the three slow precession modes for $\omega_{g12}/\Omega_1 = 0.1$. The vertical scale is arbitrary except for the condition $h^2 \ll r^2$. Smooth lines have been drawn through the calculated values indicated by circles.

Fig. 13.— Illustrative orbits $\Theta_j(t)$ for three co-rotating rings in an *oblate* halo for weak (a, top panel) and strong (b, bottom panel) coupling for the same parameters as Figure 12. The initial conditions are $\Theta_j \propto r_j$ and $\dot{\Theta}_j = 0$. The points labeled by f 's all correspond to the final time $t_f = 45\pi/\Omega_1$ (which is ar-

bitrary). For the top panel, $\omega_{g12}/\Omega_1 = 0.005$ and the rings precess almost independently. For the bottom panel, $\omega_{g12}/\Omega_1 = 0.03$ and the rings precess together with their lines-of-nodes phase-locked as shown in figure 14.

Fig. 14.— Azimuthal angles $\varphi_j(t)$ of the line-of-nodes for three rings for cases of: (a) weak ($\omega_{g12} = 0.005\Omega_1$), (b) intermediate ($\omega_{g12} = 0.015\Omega_1$), and (c) strong coupling ($\omega_{g12} = 0.03\Omega_1$).

Fig. 15.— The figure shows the power spectrum as a function of angular frequency ω of $\theta_{x25}(t)$ - the x -component tilt angle of the middle ring at $r = 25$ kpc - for a $N = 49$ ring disk given a random initial perturbation. The frequency ω is normalized by the angular velocity of the disk at r_1 , Ω_1 . The spectrum is obtained using a 1024 point FFT. The initial perturbation is taken to have a ‘white noise’ radial wavenumber spectrum; that is, all radial wavenumber modes are excited. The $\Theta_j(t)$ are obtained using a code which solves equations (55) with the rings equally spaced between $r_1 = 10$ kpc and $r_{49} = 40$ kpc. Dissipation is neglected ($\beta_j = 0 = \beta_j'$). The mass of the inner disk in equation (4) is $M_d = 6 \times 10^{10}M_\odot$, and the disk radial scale is $r_d = 4$ kpc. The halo potential is given by equation (6a) with ellipticity $\varepsilon = 0.0871$, core radius $r_o = 15$ kpc, and circular velocity $v_o = 200$ km/s. The neutral hydrogen has a total mass of $1.36 \times 10^{10}M_\odot$ and is distributed according to equation (5) with $R_H = 20$ kpc. The separation between low and high frequency modes is roughly at $\omega/\Omega_1 = 0.75$. The lowest frequency of the spectrum is $|\omega_1|/\Omega_1 \approx 0.0368$ while the next two higher frequencies are at ≈ 0.0521 and 0.0639 . Note that the limiting value of ω_1 from the generalization of equation (47) is $\omega_1 \rightarrow \sum L_j \omega_{pj} / \sum L_j \approx -0.120\Omega_1$ which is significantly larger in magnitude than the ω_1 observed.

Fig. 16.— The top panel (a) shows a polar plot (a Briggs plot) of the tilt angle of the disk θ in degrees as a function of the angle of the line-of-nodes φ for the case of a retrograde passage of a compact satellite for times $t = 1, 2, \text{ and } 3$ Gyr after the time of closest approach. The plot shows a *leading* spiral wave qualitatively of the form observed, but with a relatively small amplitude compared with many observed warps (Briggs 1990).

– The bottom panel (b) shows a comparison of the disk response with and without gravitational interac-

tion (C_{jk}) between the rings. This figure shows the locking of the phase φ in the inner part of the disk.

– The results shown in (a) and (b) are obtained from a code which solves equations (55) including the torques of equation (59) with $N = 49$ rings equally spaced between $r_1 = 10$ kpc and $r_{49} = 40$ kpc. Thus the separation between rings is $\Delta r = 0.625$ kpc. The torques are evaluated numerically at each time step. The Newtonian drag is neglected, $\beta_j = 0$ in equation (56). A small relative friction is included, $\beta'_j/\Omega_1 = 0.02$ in equation (57). [For a disk half-thickness $\Delta z = 250$ pc and sound speed $c_s = 10$ km/s, this β'_j corresponds to a value of Shakura’s (1973) viscosity parameter $\alpha \approx 0.0624$. This friction acts to smooth out sharp ‘corners’ which exist in the $\beta'_j = 0$ curve $\theta(\varphi)$. Owing to this β'_j , \mathcal{E}_{rings} decreases by 16% between $t = 1$ and 3 Gyr.] The mass of the satellite is $2 \times 10^{10} M_\odot$, its core radius is $a = 1$ kpc, and at closest approach it is at a distance $r_{so} = 30$ kpc where it has a speed of 400 km/s and is located at an angle 30° above the (x, y) plane. The mass of the inner disk in equation (4) is $M_d = 6 \times 10^{10} M_\odot$, and the disk radial scale is $r_d = 4$ kpc. The halo potential is given by equation (6a) with ellipticity $\varepsilon = 0.0871$, core radius $r_o = 15$ kpc, and circular velocity $v_o = 200$ km/s so that $(\kappa_{hz}^2 - \Omega_h^2)/\Omega_h^2 = 0.2$ for $r^2 \gg r_o^2$. The mass of halo matter inside of $r = 30$ kpc is $7.4 \times 10^{10} M_\odot$. The neutral hydrogen has a total mass of $1.36 \times 10^{10} M_\odot$ and is distributed according to equation (5) with $R_H = 20$ kpc.

Fig. 17.— The top panel (a) shows a polar plot of the tilt angle of the disk θ in degrees as a function of the angle of the line-of-nodes φ for the case of a prograde passage of a compact satellite at times $t = 1$ and $t = 4$ Gyr after the time of closest approach. The other conditions are the same as given in the caption to Figure 16. The plot shows that initially ($t = 1$ Gyr) a *trailing* spiral wave is formed. Later, ($t = 4$ Gyr) the trailing wave ‘unwraps’ and gives rise to a *leading* spiral wave. Analysis of the evolution of the tilt excited by the prograde satellite shows that it is initially a *fast* outward propagating wave with radial phase velocity $v_r^{ph} \approx 24$ km/s and radial wavelength $\lambda_r \approx 11$ kpc for $r \sim 25$ kpc. Roughly, $\lambda_r \propto r^{2.5}$.

– The bottom panel (b) shows a comparison of the orbits [$\theta_{25x}(t)$, $\theta_{25y}(t)$] (in degrees) of ring No. 25 at radius $r_{25} = 25$ kpc for $t = 0 - 1$ Gyr for the cases of retrograde and prograde satellite encounters for the conditions of Figures (15a) and (16a). The circles and squares are equally spaced at 0.1 Gyr intervals.

The (i) indicates $t = 0$ and the (f’s) correspond to $t = 1$ Gyr. For the retrograde case, mainly the slow precession mode of the ring is excited, whereas for the prograde case mainly the fast precession mode is initially excited.

Fig. 18.— The top panel (a) shows a polar plot of the tilt angle of the disk θ in degrees as a function of the angle of the line-of-nodes φ for the case of a retrograde sinking of a compact minor satellite of mass $M_s = 10^{10} M_\odot$ at times $t = 2$ and $t = 4$ Gyr after the sinking ($\mathbf{r}_s = 0$). Initially, the rings are unperturbed and the satellite is ‘turned on’ at a distance $r_s = 50$ kpc in the (x, z) plane 30° above the (x, y) plane. The in-spiral of the satellite is described by equation (60a) with $\ell n \Lambda = 3$. The other conditions are the same as described in the caption of Figure 16 except that the relative friction is larger, $\beta'_j/\Omega_1 = 0.2$. The Newtonian drag is neglected. This value of β'_j has the effect of damping out short radial wavelength features of the tilt while not appreciably changing the overall $\theta(\varphi)$ curve.

– The bottom panel (b) shows the Briggs plot for a prograde sinking for conditions otherwise the same as in (a) above.

Fig. 19.— The top panel (a) shows the Laplacian tilt angle of the rings $\Theta_j^L = \theta_{jx}^L$ with and without self-gravity of the rings (C_{jk}) for the case where the halo potential [equation (6a)] is rigidly tilted by an angle $\Theta_h = \theta_{hx} = 30^\circ$ with respect to the z -axis of the inner disk of the galaxy. The disk and halo are the same as in Figure 16. The Θ_j^L are obtained by solving equation (62).

– The bottom panel (b) shows the Briggs plots for the Laplacian tilt and that for a small initial deviation from a Laplacian tilt at times $t = 4$ and 8 Gyr. The initial deviation is taken to be $\Theta_j = \theta_{jx}^L \{1 + 0.2 \sin[\pi(r_j - r_1)/2(r_N - r_1)]\}$. This deviation vanishes at $r_j = r_1$ and it has a maximum at the outer edge of the disk. Dissipative torques are neglected. This deviation from Θ_j^L gives rise to a leading spiral feature at the outer edge of the disk at $t = 8$ Gyr. For a deviation with the +0.2 factor replaced by -0.2 the line-of-nodes angle at the outer edge of the disk (φ_{49}) at $t = 8$ Gyr has a similar magnitude to that in Figure 19b, but it is negative.

Fig. 20.— The top panel (a) shows the radial dependence of the tilt angle $\theta(r)$ for different times after the initial time ($t = 0$) when the disk tilt is give by

equations (63) with outer disk tilt angle $\theta_{xo} = 30^\circ$. The conditions of the disk and halo are otherwise the same as for Figure 16.

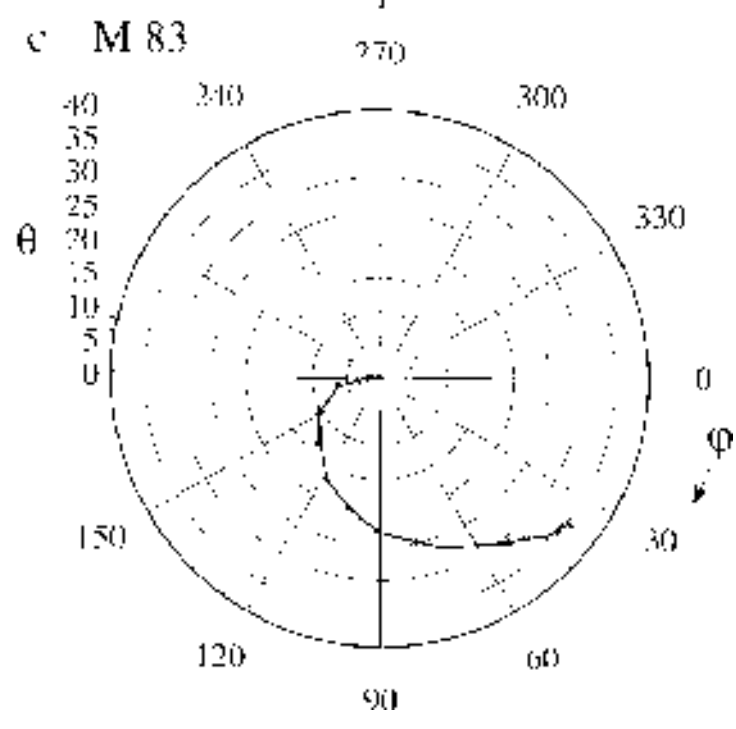
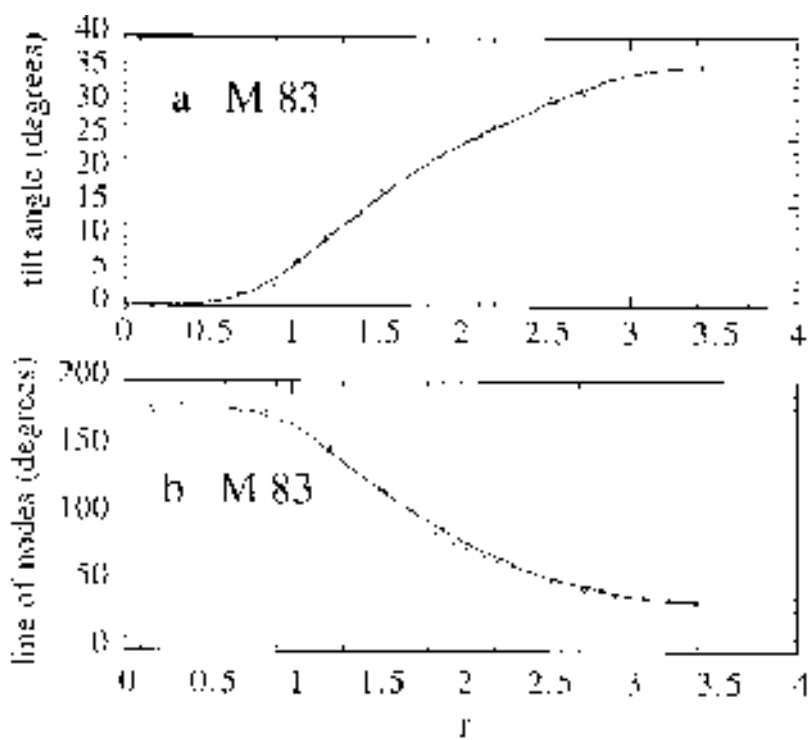
–The middle panel (**b**) shows the radial dependence of the line-of-nodes $\varphi(r)$. The constant value of $\varphi(r)$ in the inner part of the disk results from phase-locking due to the self-gravity of the rings as discussed in §2.3 and §2.5. The dashed curves correspond to least-square fits of a power law to $\varphi(r)$. For $t = 2$ Gyr, the fit gives $\varphi = 498^\circ r^{-1.42}$ for $r = 23 - 40$ kpc (with an R value of 0.96). For $t = 4$ Gyr, the fit gives $\varphi = 1680^\circ r^{-1.79}$ for $r = 28 - 40$ kpc (with an R value of 0.97). Note that for M 83 (Figure 2b), the least-square fit gives $\varphi = 216^\circ r^{-1.48}$.

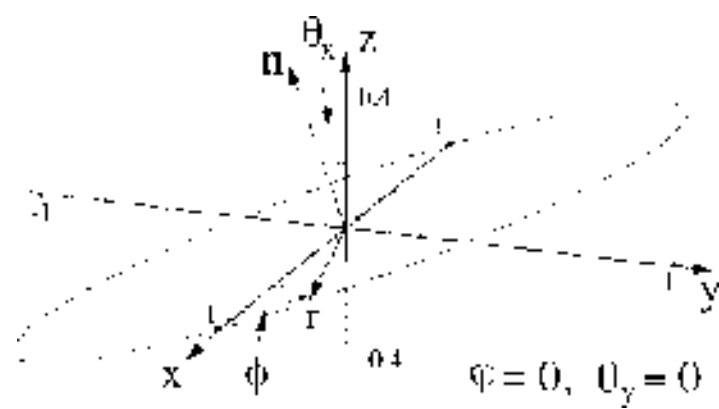
– The bottom panel (**c**) shows the Briggs plots for a sequence of times. A leading spiral wave forms, and its amplitude grows with time. The $\theta(\varphi)$ spiral for $t = 2 - 4$ Gyr is qualitatively similar to that observed for M 83 (see Figure 2c). From results not shown here the similarity continues up to $t \sim 6$ Gyr after which time θ and $d\theta/dr$ become large at the outer edge of the disk. The present theory assumes small tilting amplitudes $\theta^2 \ll 1$ for the linearization of the equations of motion. The linearity allows an arbitrary rescaling $\Theta_j \rightarrow K\Theta_j$ with $K = \text{Const.}$ (or $\theta_j \rightarrow K\theta_j$ and $\varphi_j \rightarrow \varphi_j$) in Figure 20.

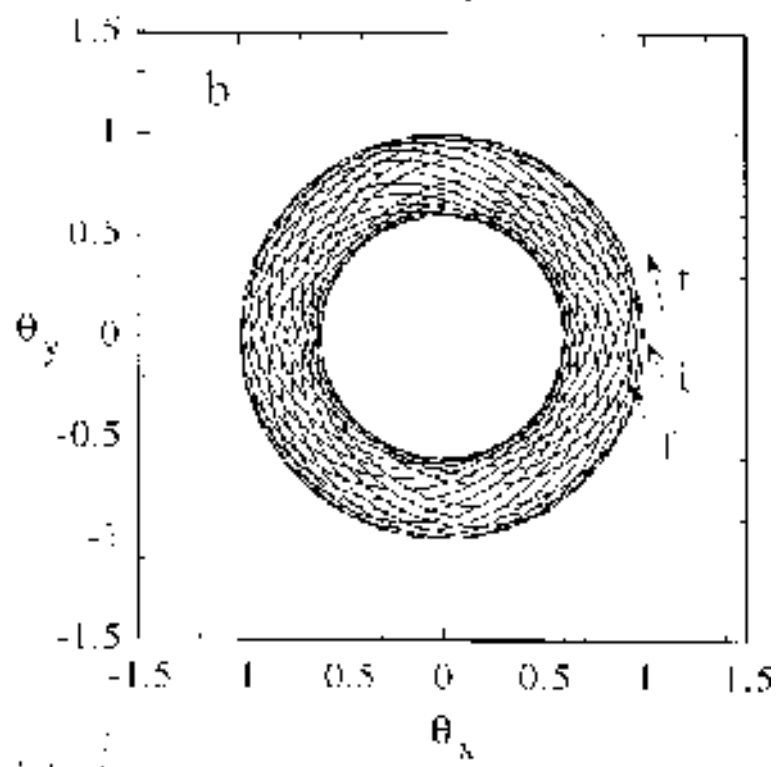
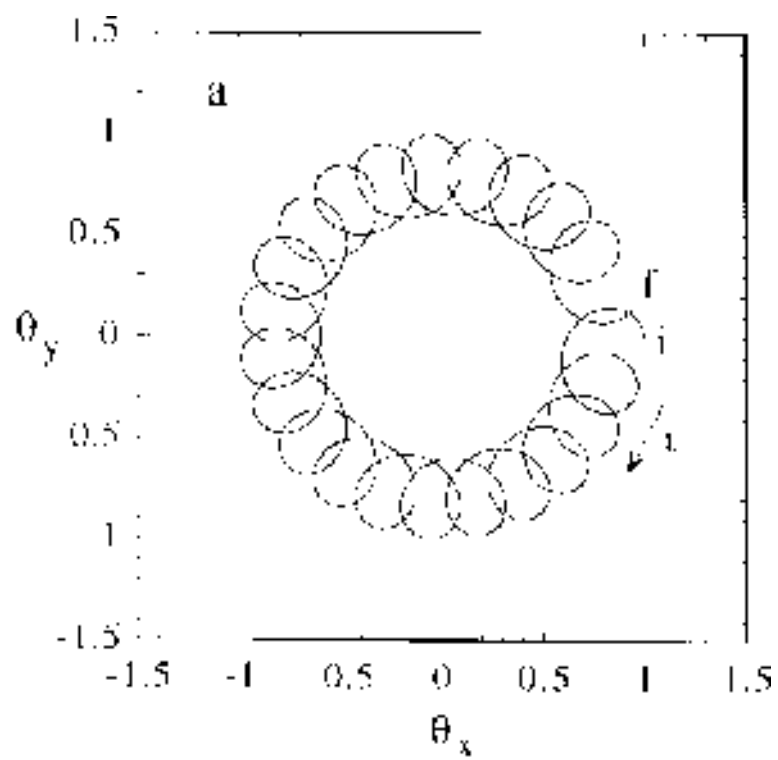
Fig. 21.— Surface plot of the warped disk of Figure 20 at $t = 2$ Gyr. To facilitate comparison with Figure 1 for M 83, the rotation of the disk has been taken to be clockwise in this figure. The warp is a leading spiral wave the same as for M 83. The colors are in 16 steps uniformly spaced between z_{min} and z_{max} .

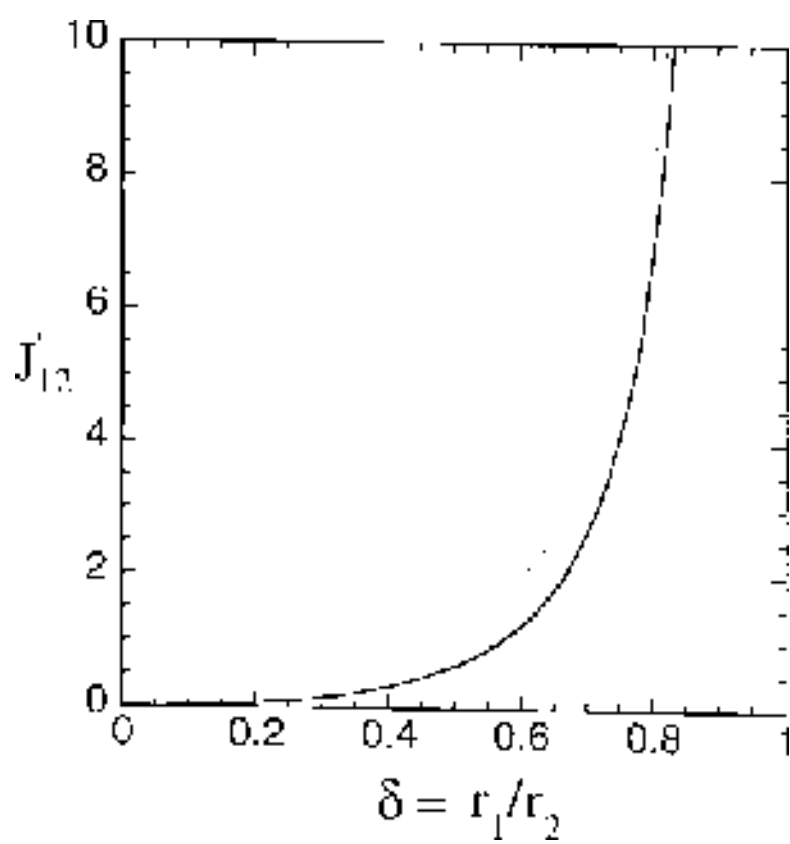
This figure "Fig1RL.jpg" is available in "jpg" format from:

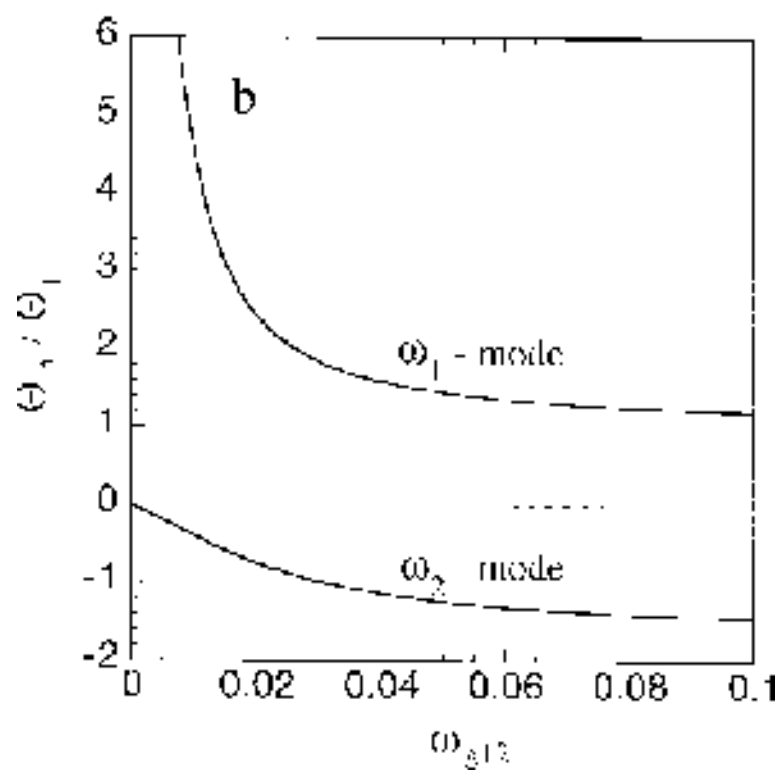
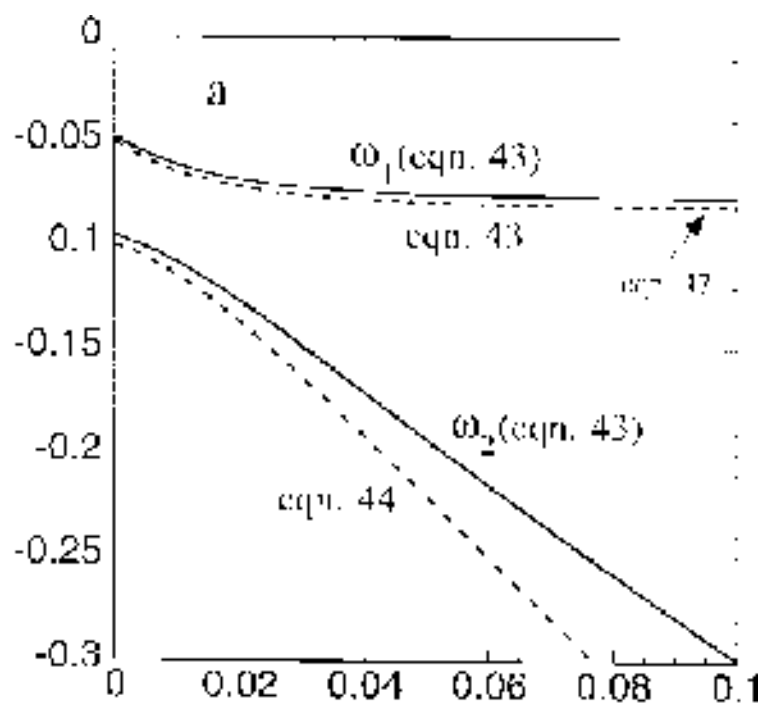
<http://arxiv.org/ps/astro-ph/9707227v1>

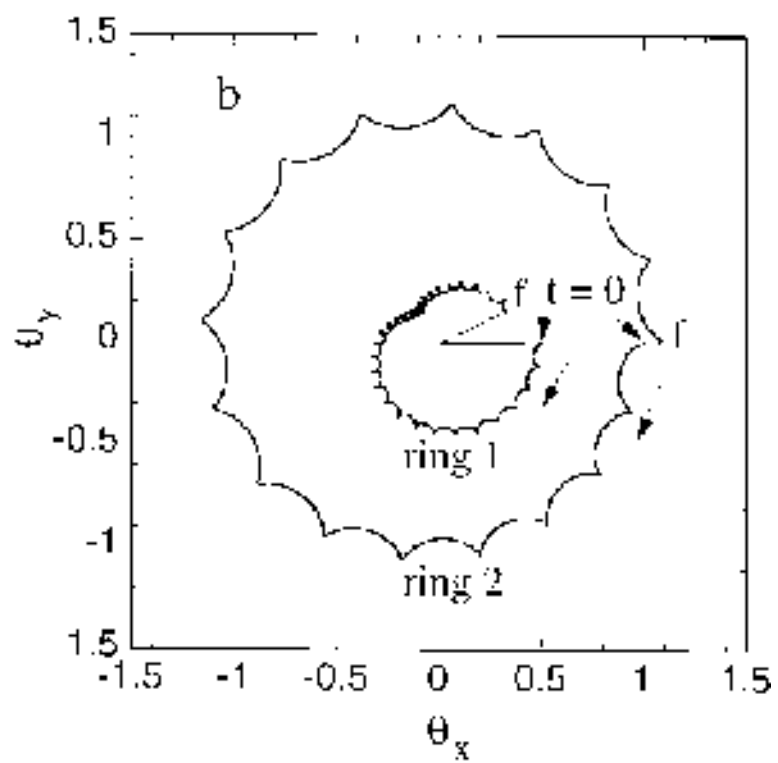
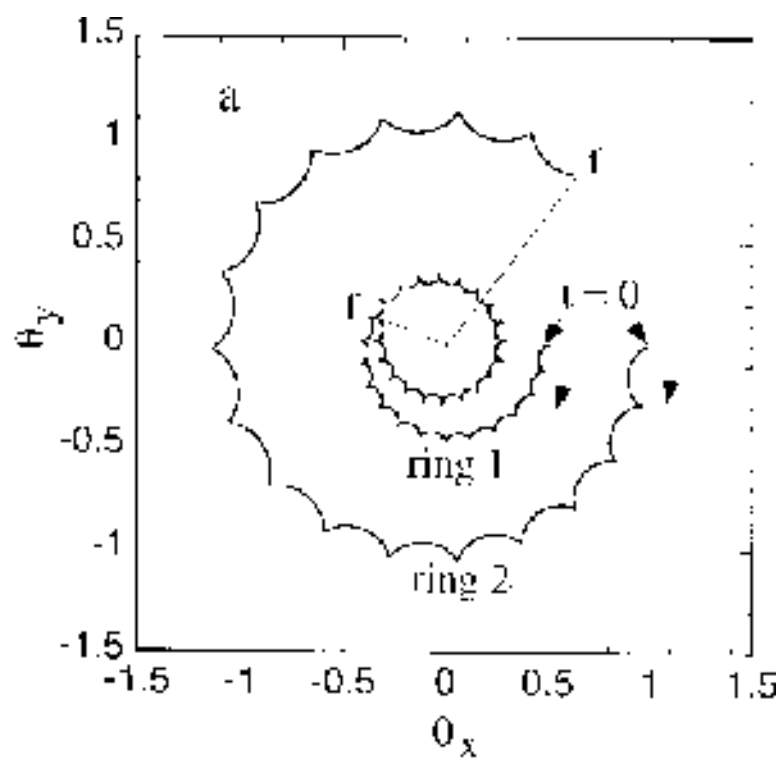


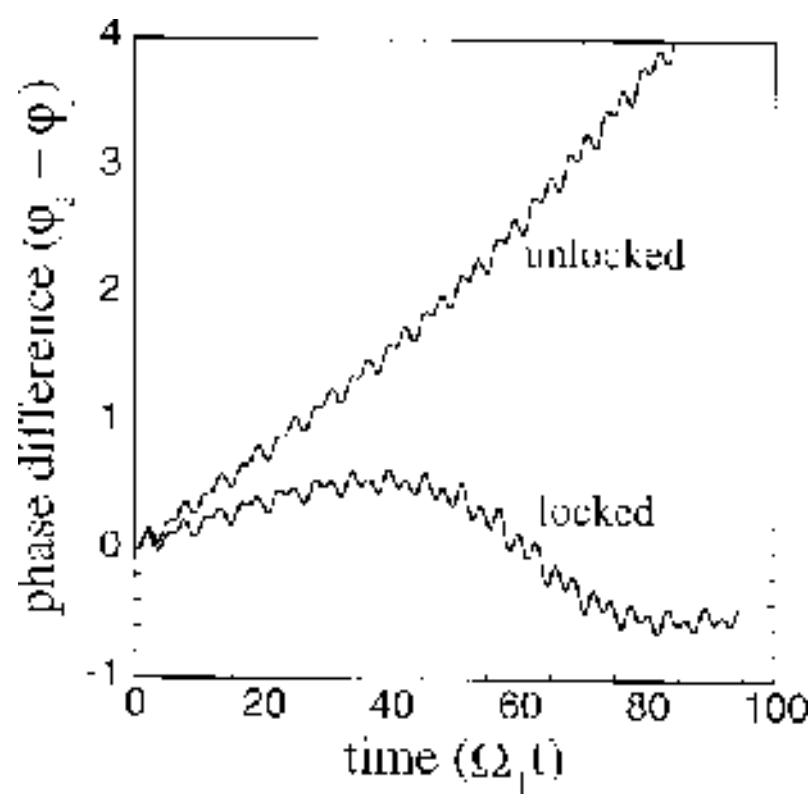


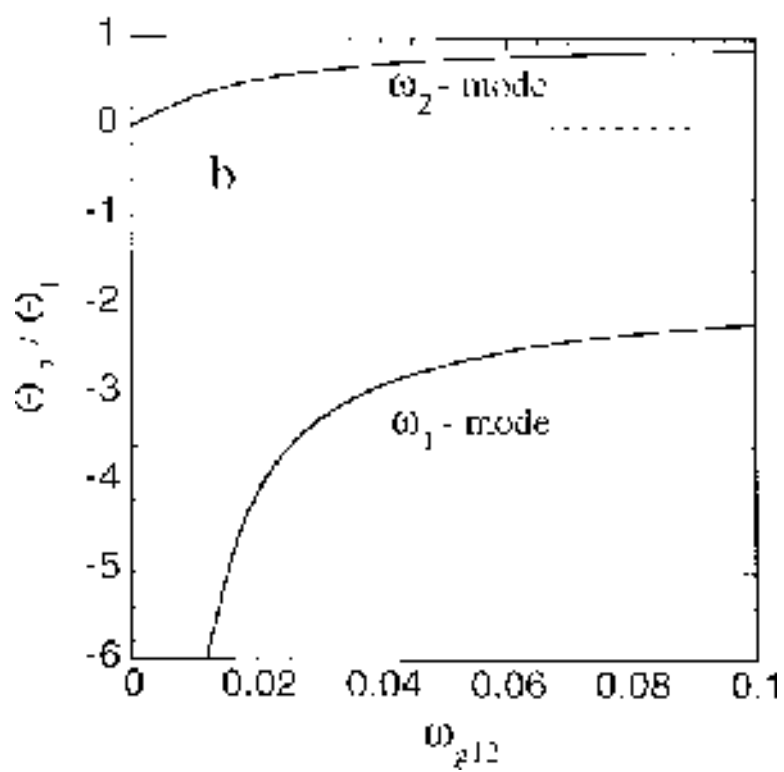
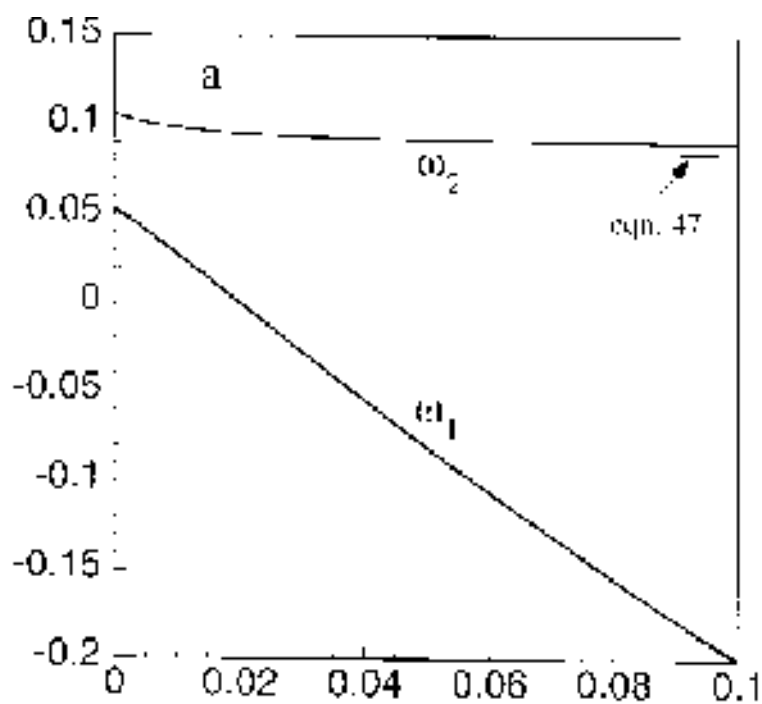


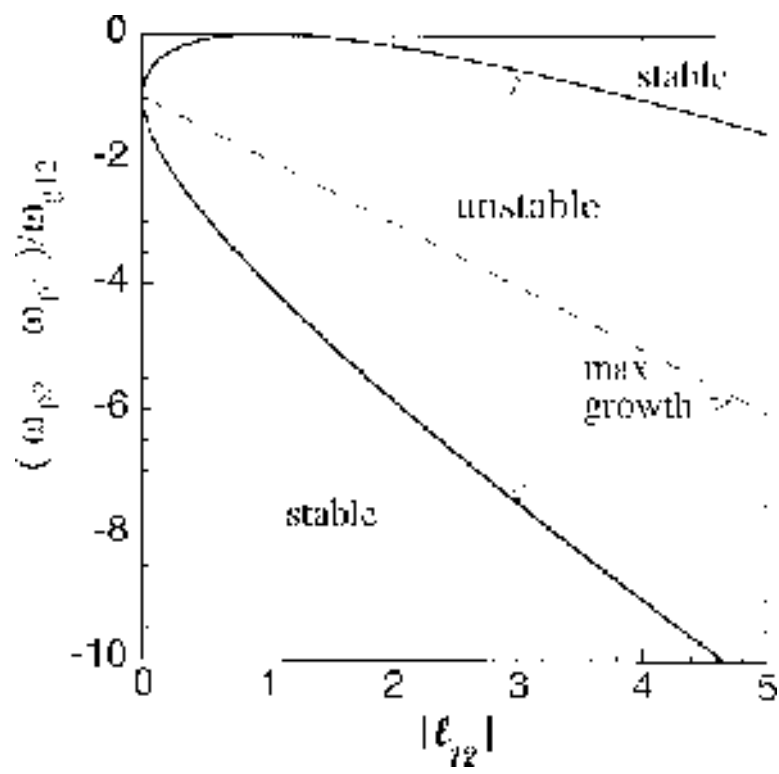


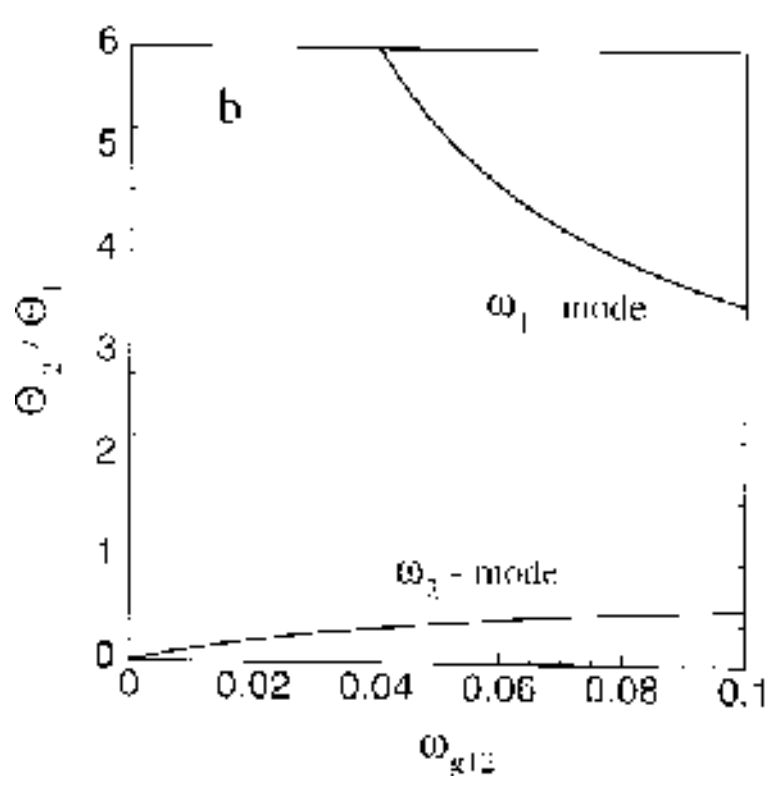
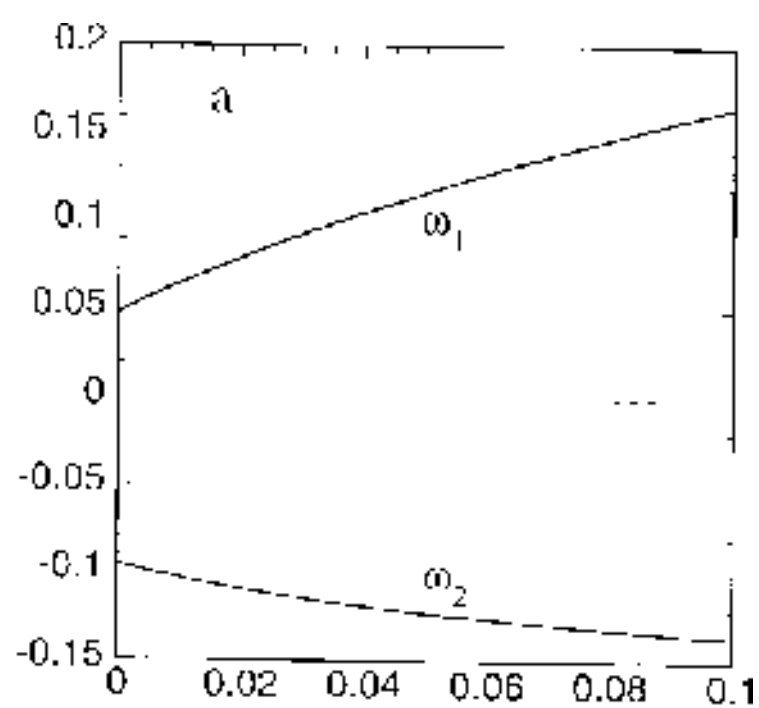


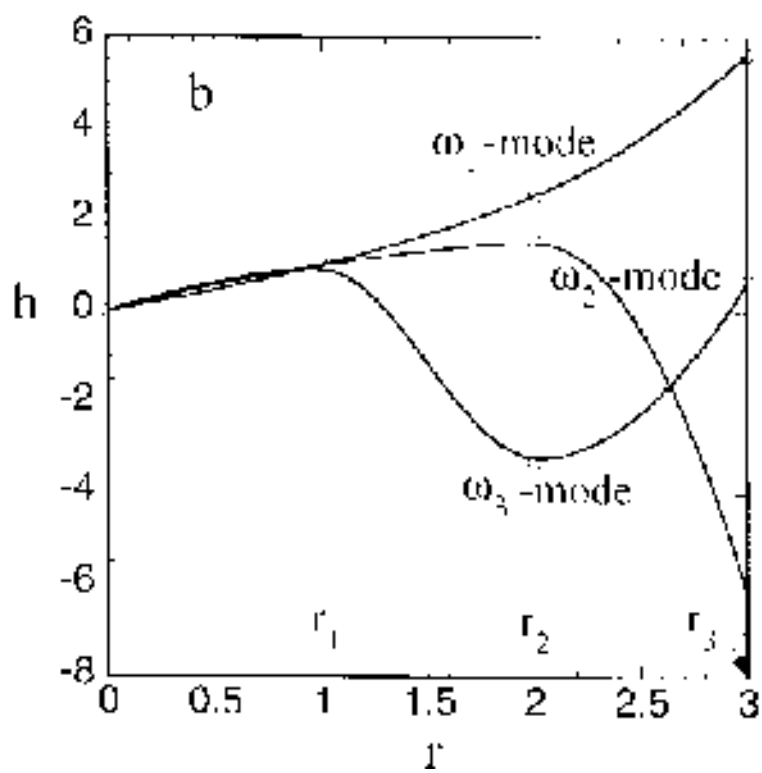
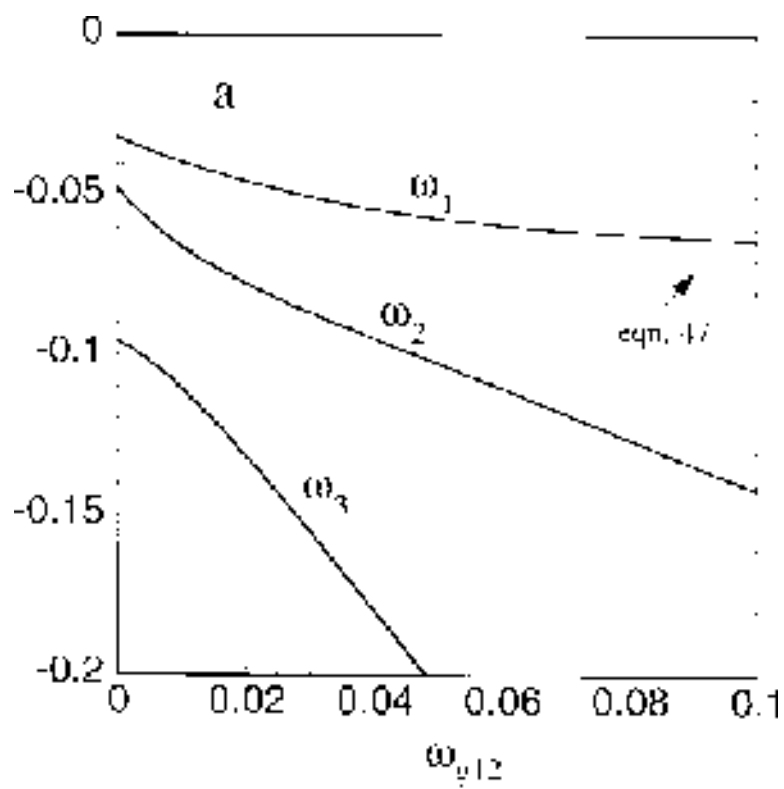


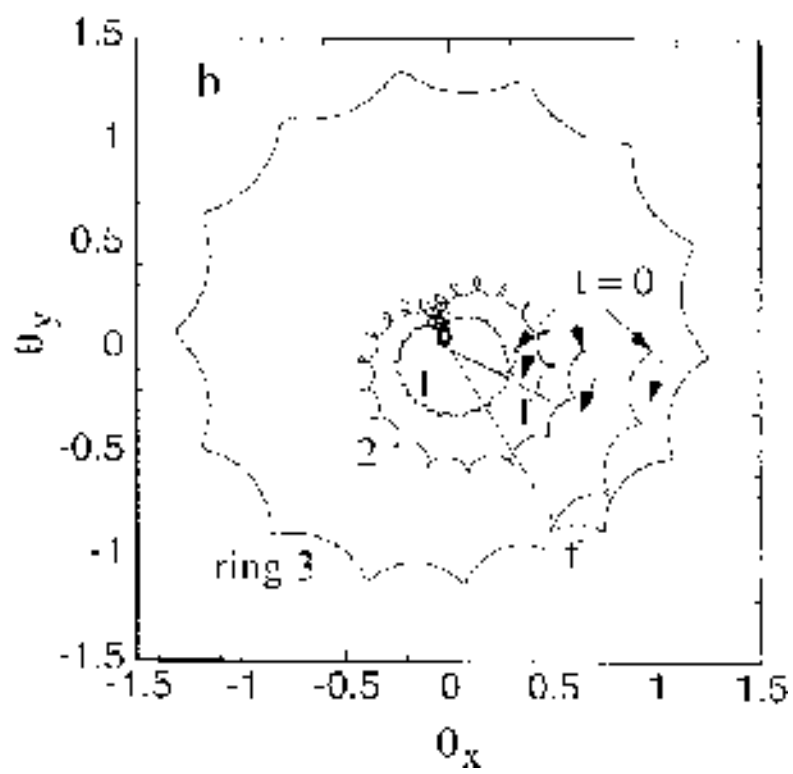
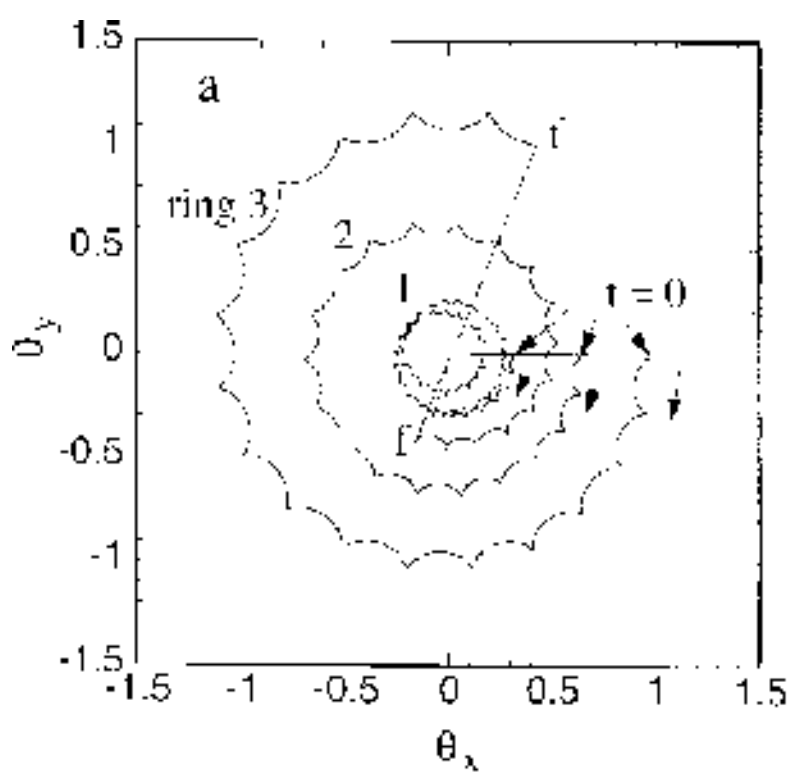


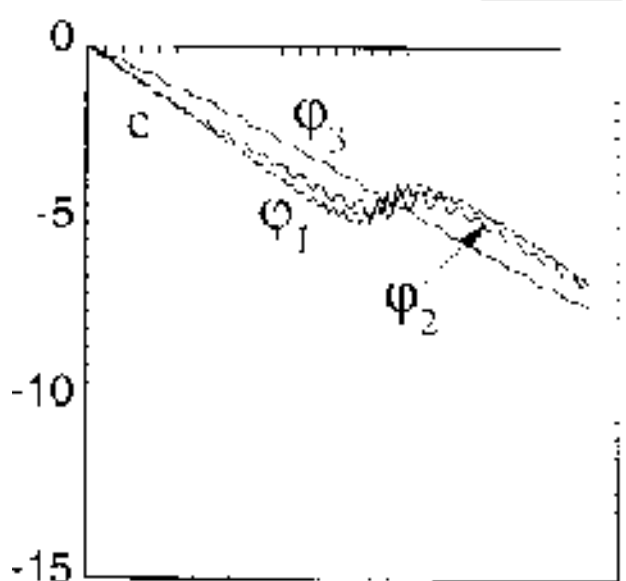
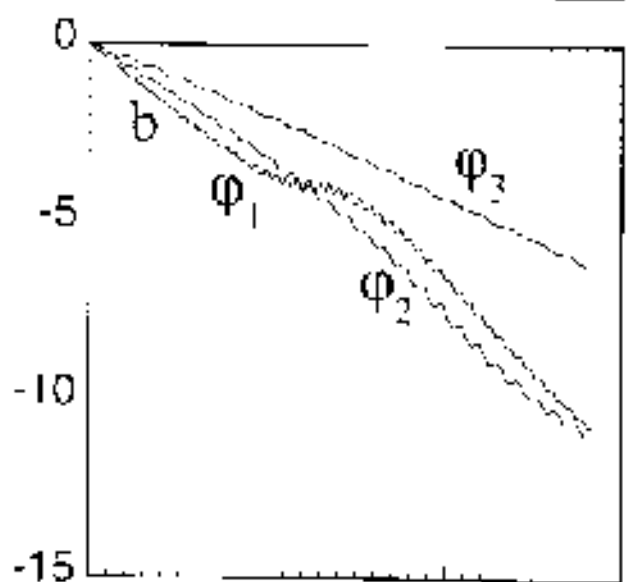
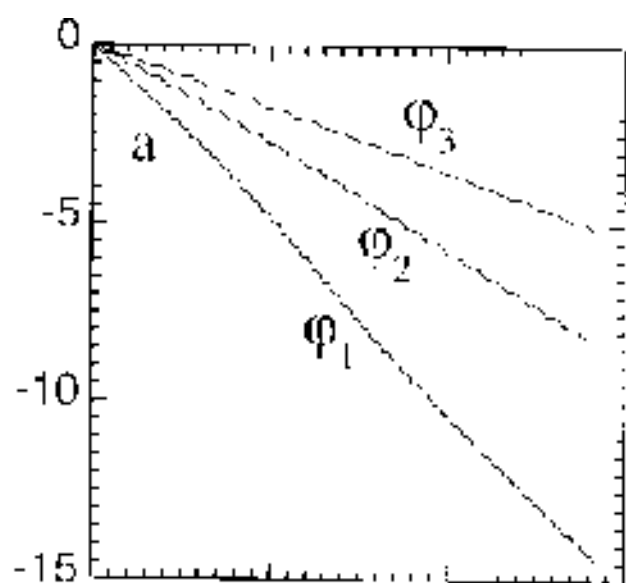




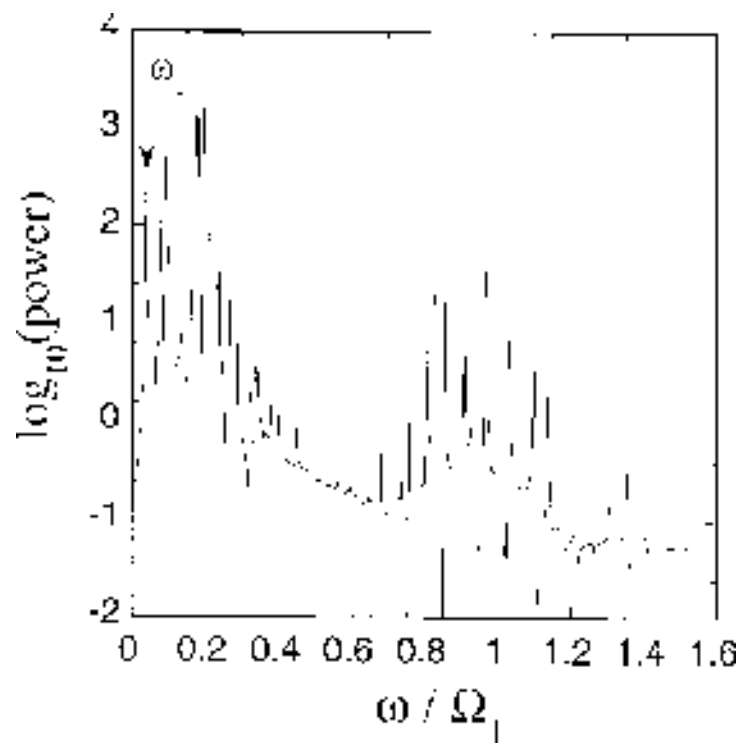




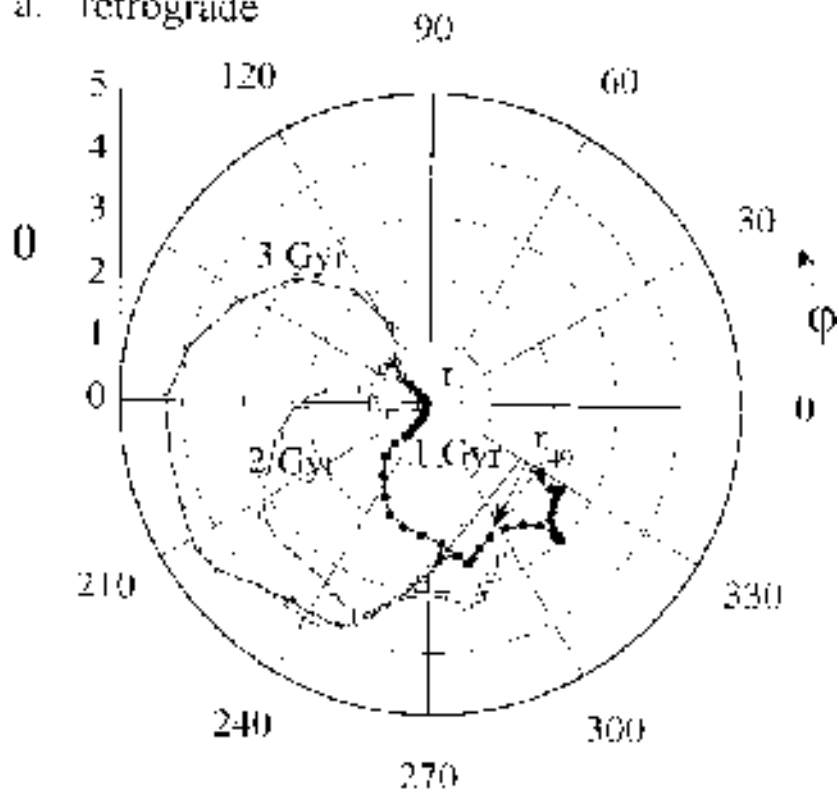




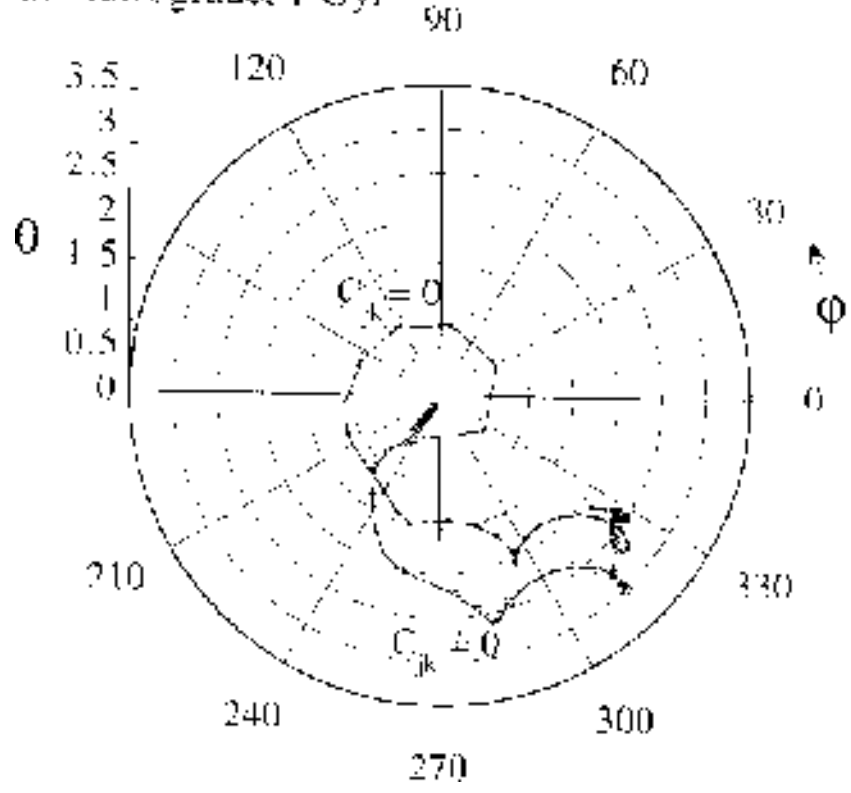
time ($\Omega_1 t$)



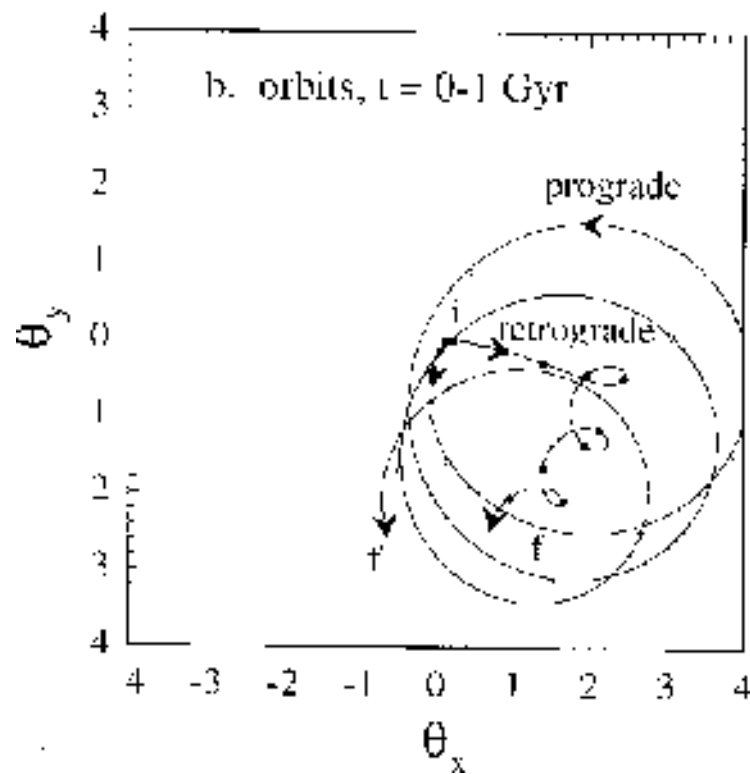
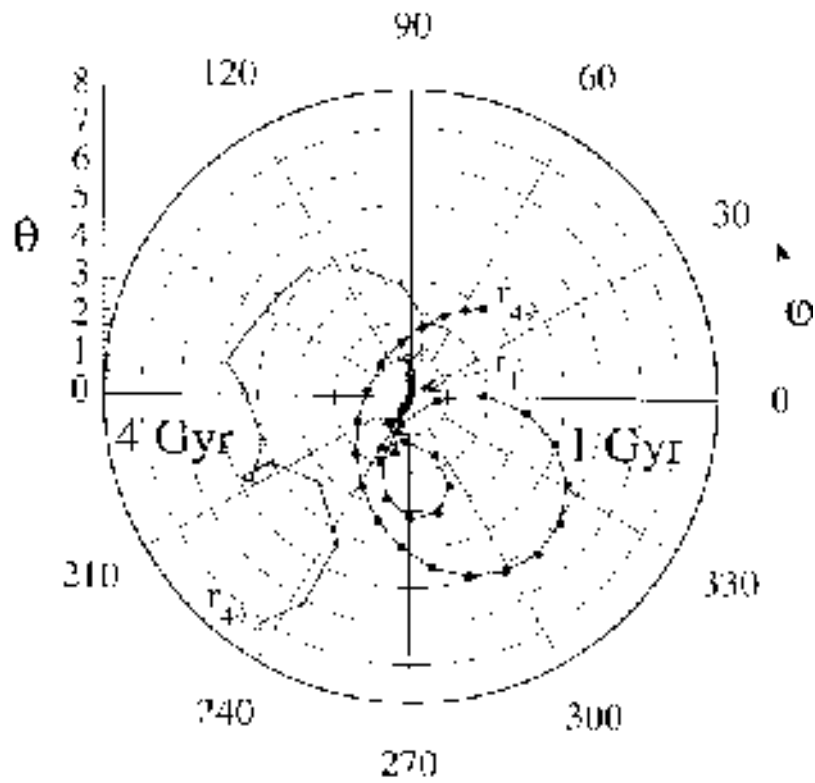
a. retrograde



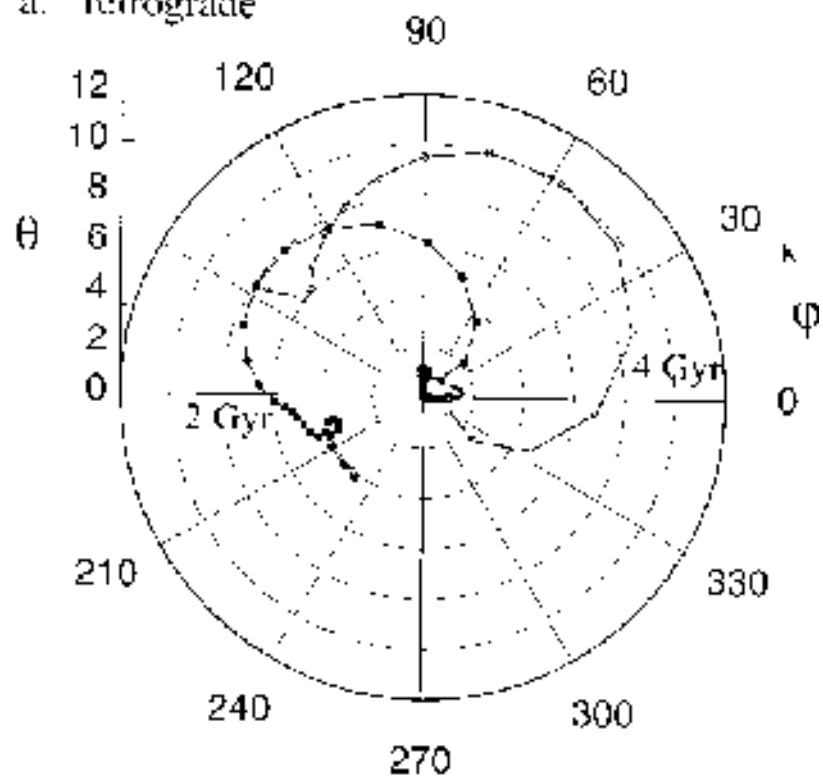
b. retrograde, 1 Gyr



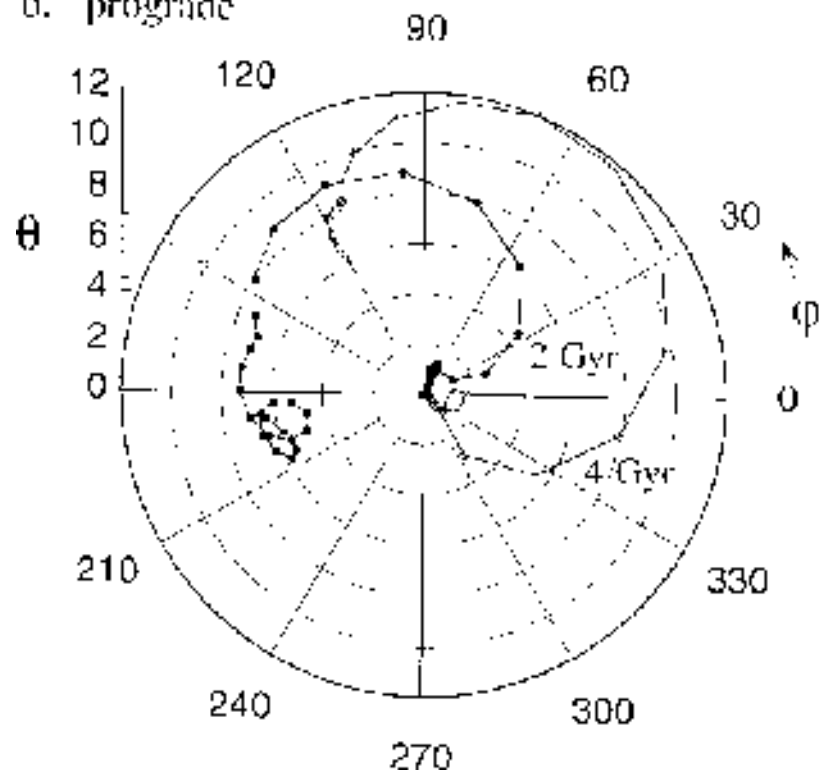
a. prograde



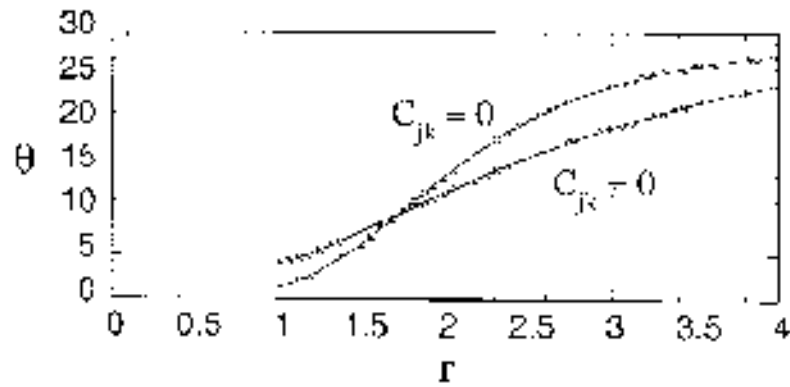
a. retrograde



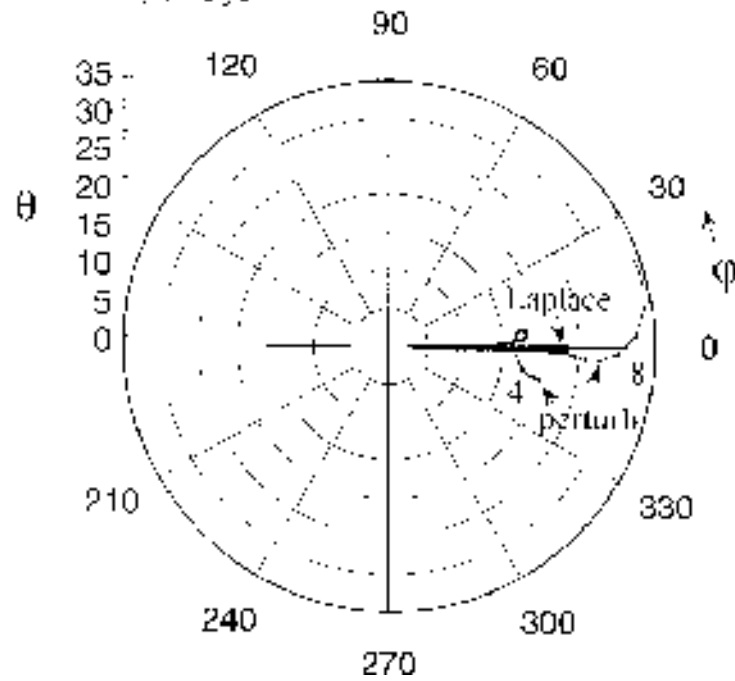
b. prograde

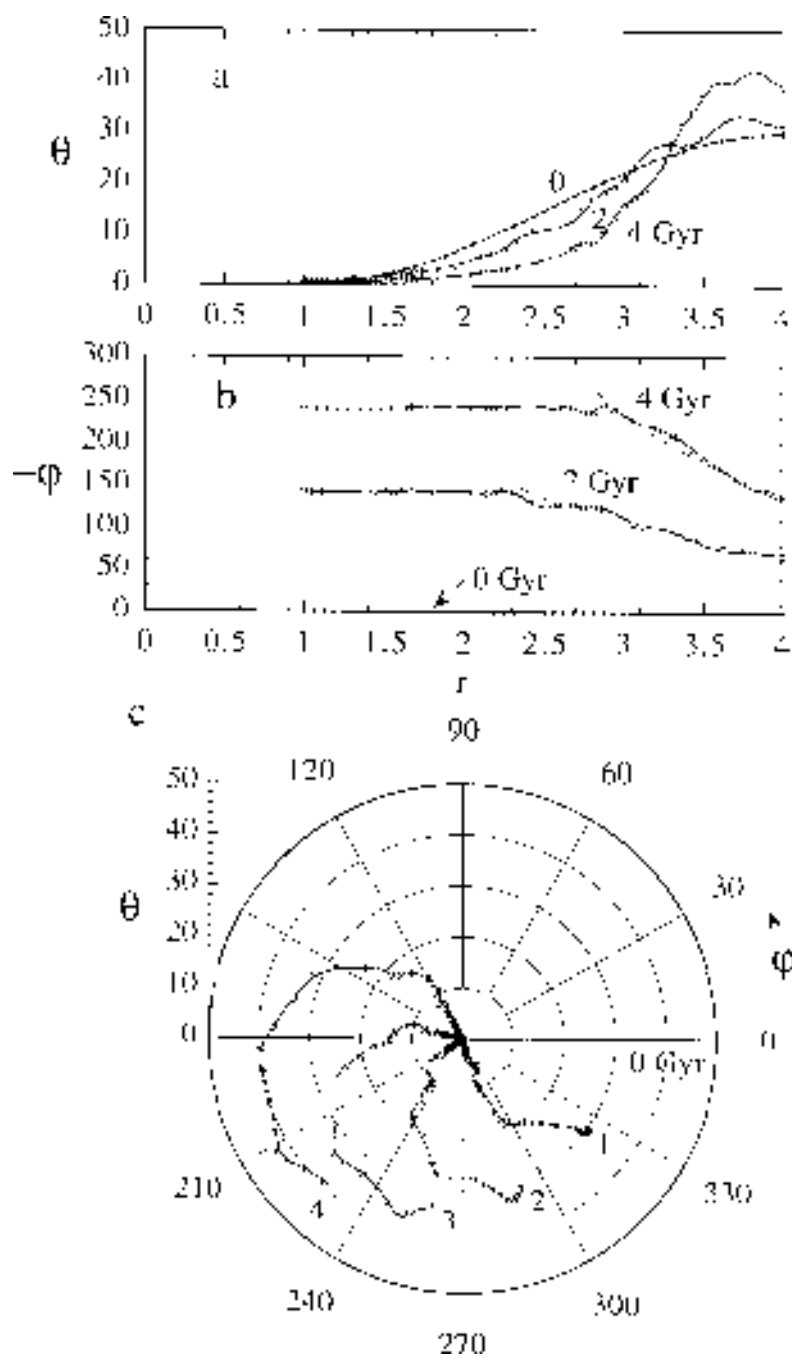


a. Laplacian warp



b. $\tau = 4, 8$ Gyr





This figure "Fig21RL.jpg" is available in "jpg" format from:

<http://arxiv.org/ps/astro-ph/9707227v1>